THESIS FOR THE DEGREE OF LICENTIATE OF ENGINEERING

Organic functionalization of graphene for applications in energy storage devices and optoelectronics

Cheng Peng

Department of Chemistry and Chemical Engineering

CHALMERS UNIVERSITY OF TECHNOLOGY

Gothenburg, Sweden 2024

Organic functionalization of graphene for applications in energy storage devices and optoelectronics

Cheng Peng

Technical report No.2024:07

Department of Chemistry and Chemical Engineering

Chalmers University of Technology

SE-412 96

Göteborg

Sweden

Telephone + 46 (0)31-772 1000

Gothenburg, Sweden 2024

Organic functionalization of graphene for applications in energy storage devices and optoelectronics

Cheng Peng

Department of Chemistry and Chemical Engineering

Chalmers University of Technology

Abstract

The emergence of one-atom layer thick materials, exemplified by graphene following its first exfoliation by Geim and Novoselov, has sparked significant research interest. Owing to their unique electronic structure, 2D materials are regarded as promising candidates for diverse applications, including field-effect transistors (FETs), solar energy harvesting, biological systems, water purification, and energy storage devices. It has been demonstrated that the introduction of functional molecules onto the surface of 2D materials not only prevents the aggregation of the nanosheets but also enables fine-tuning of their physicochemical properties.

The widespread use of fossil fuels has propelled human society into a period of rapid industrial development. However, this progress has come with significant environmental challenges and concerns over the depletion of fossil energy sources. As a result, there is a pressing need for humanity to transition towards sustainable energy alternatives. Lithium-ion batteries (LIBs), as the predominant energy storage device in our daily lives, face limitations such as low power density, safety issues, and resource dependency. Aqueous supercapacitors utilizing 2D materials offer a promising solution to address these challenges. For instance, employing aqueous electrolytes can significantly enhance the safety of energy storage devices. In this thesis, we have developed asymmetric supercapacitors using graphene functionalized with pyrenetetraone derivatives as cathode and annealed $Ti_3C_2T_x$ as anode, demonstrating a remarkable energy density of 38.1 Wh kg^{-1} at a power density of 950 W kg^{-1}. Additionally, they exhibit outstanding stability, retaining more than 90% capacity after 15000 charge/discharge cycles. Furthermore, spectrophotometric titration was deployed to reveal the different interaction behaviors within the different functionalized 2D-materials. The rationally designed organic nanostructures exhibited excellent electrochemical performance, offering valuable insights in the design of organic-based electrode materials.

In addition, donor-acceptor system based on pyrenetetraone derivatives is designed and synthesized for the noncovalent functionalization of graphene. Further photophysical investigation on the hybrid material confirmed the interaction between the donor-acceptor system and graphene.

Keywords: 2D materials, graphene, organic functionalization, aqueous energy storage, optoelectronics

List of publications

This thesis is based on the following publications:

I. A Novel Aqueous Asymmetric Supercapacitor based on Pyrene-4,5,9,10-Tetraone Functionalized Graphene as the Cathode and Annealed $Ti_3C_2T_x$ MXene as the Anode.
M. Shi, C. Peng, X. Zhang
Small **2023**, 19, 2301449.

II. Aqueous Asymmetric Supercapacitors with Pyrenetetraone-Derived Pseudocapacitive Polymer-Functionalized Graphene Cathodes Enabling a 1.9 V Operating Window.
C. Peng, C. Guo, Y. Wang, Y. Li and X. Zhang
Adv. Energy Sustainability Res. **2024**, 5, 2300217.

Contributions to the publications:

Paper I: Synthesis of pyrenetetraone, XPS and SEM measurements of the resulting nanocomposites.

Paper II: Synthesis, characterization of the materials, data analysis and manuscript drafting. Theory calculations were performed by the collaborator.

Abbreviations

ASC	Asymmetric supercapacitor
EES	Electric energy storage
EDLC	Electric double-layer capacitor
GO	Graphene oxide
rGO	Reduced graphene oxide
CV	Cyclic voltammetry
GCD	Galvanic charge-discharge
PAH	Pericyclic aromatic hydrocarbon
PYT	4,5,9,10-pyrenetetraone

Contents

1. Introduction and background

1.1. Graphene

In the early 16th century, graphite was initially discovered in Cumbria, North England.[1] Its value soared when it was identified as an exceptional mold for producing cannonballs. Graphite mining became a state-owned enterprise in the United Kingdom for a time.[2] Following its documented use as a pencil in 1656, graphite became widely utilized as an art material across Europe. In 1789, it was named "graphite" by Abraham Gottlob Werner, derived from the Greek "graphein," meaning 'to write.' Apart from its function as a writing tool, graphite serves various other roles in modern life, including as electrodes, lubricants, hardeners in steelmaking, and moderators in the nuclear industry.

The initial exfoliation of graphene from crystalline graphite via the Scotch-tape procedure, pioneered by Andre Geim and Kostya Novoselov, represented a significant milestone in the realm of 2D materials.[3] Following this breakthrough, graphene emerged as the centerpiece of interdisciplinary research. Renowned as the best-studied 2D material, graphene possesses a honeycomb-like structure with a one-atom-thick layer lattice, making it the thinnest and strongest material known.[4] Meanwhile, it shows excellent thermal and electrical conductivity,[5-6] ambipolar field effect,[7] large specific area,[8] and high transparency.[9] Thanks to these fantastic properties, graphene has been used for various potential applications, including field-effect transistors (FETs),[10] solar energy harvesting,[11] biological systems,[12] water purification,[13], and energy storage devices.[14-15]

Different preparation methods have been developed to obtain graphene, which can be classified into ‘top-down’ and ‘bottom-up’ methods. In top-down processes, graphene is produced from the bulk graphite via mechanical cleavage, electrochemical exfoliation,[16] liquid phase exfoliation,[3, 17] reduction of graphene oxide (GO),[18-20] and arc-discharge method.[21] As for the bottom-up approaches, graphene can be produced by molecular growth from small molecules via chemical vapor deposition,[9, 22-23] organic synthesis,[24] pyrolysis,[25] and epitaxial growth on SiC.[26]

Despite these fantastic properties, graphene is also considered a zero-bandgap semiconductor, which hinders its application in FETs. Also, pristine graphene has limited dispersibility in solvents. These challenges have prompted researchers to explore both covalent and noncovalent approaches for functionalizing graphene and its derivatives. Introducing

functional groups has the potential to imbue graphene with new properties, thereby expanding its range of applications.

1.2. 2D materials beyond graphene and the energy storage of MXene

The discovery of graphene simulated the interests of study in other 2D materials, which also show sheet-like nanostructures. The emerging 2D materials such as transition metal dichalcogenides (TMDs), graphitic carbon nitride, MXenes, black phosphorus, hexagonal boron nitride, and transition metal oxide (TMOs) have been considered promising candidates for applications in transistors, optoelectronics, sensors, and supercapacitors.[27-32]

MXene is a family of 2D materials with the chemical formula of $M_{n+1}X_nT_x$, where M represents a transition metal, X denotes carbon or/and nitrogen, and T signifies terminal groups such as -OH, -F/Cl/Br.[33] The transition metal layer endows MXene's excellent conductivity and charge transfer capability. In addition, transition metals usually show different oxidation numbers along the stacked structure. These above properties render MXene attractive in energy storage applications. In this thesis, the most representative MXene species, titanium carbide ($Ti_{n+1}C_nT_x$), was used as anode in aqueous supercapacitors.

1.3. Functionalization of graphene

As the most extensively studied 2D material, graphene and its derivatives have been subject to various functionalization methods. These methods can be classified into covalent approach and noncovalent approach. Covalent approaches can provide a stable connection between the functional groups and graphene, which can also destroy the aromatic system of graphene. The reactions include but are not limited to cycloaddition,[34-35] diazonium reaction,[36] nitrene addition,[37] and Friedel-Crafts reaction.[38-39]

Noncovalent approaches are achieved by van der Waals forces, π interactions, electrostatic or hydrogen bonding forces.[40-41] Compared with covalent approaches, noncovalent functionalization can adjust the electronic properties of graphene while retain its aromatic character.

1.4. Asymmetric supercapacitors

The demand for sustainable energy is increasing due to the fossil energy shortage and growing environmental problems. [42-43] Exploring renewable resources such as solar, hydrogen, wind, and tidal can offer a promising solution to address this issue.[44-45] Electric energy serves as a crucial medium for transforming sustainable energy into the fabric of modern society, facilitating both production processes and daily life activities. According to the Sustainable

Development Goals Report 2022 from the United Nations, over 700 million people lack reliable electricity access.[46] Addressing this issue requires electric energy storage (EES) devices that are efficient, affordable, and reliable.[47] Meanwhile, the electric vehicle and consumer electronics industries must also prioritize safety, lightness, and flexibility in their products.[48] Among the EES devices, batteries and supercapacitors are the most representative energy storage technologies.[49-50] For all the electrochemical energy storage devices, the performance of which can be evaluated in two dimensions – energy density and power density. Energy density refers to the amount of energy that can be stored per unit of weight or volume, indicating the device's storage capacity. Power density, on the other hand, represents the power output per unit volume or weight. The relationship between energy density (in Wh kg^{-1}) on the y-axis and power density (in W kg^{-1}) on the x-axis of various energy storage devices is shown in Figure 1.1. This graphical representation is commonly known as the Ragone plot.[51] Nonetheless, the highly flammable electrolyte and dendrite formation during high-power charge/discharge processes not only present safety hazards such as leakage, combustion, and explosion but also shorten the cycle life of LIBs.[52-53] These issues have persisted in society since the advent of commercial LIBs and continue to be relevant today. As a complementary technology to batteries, aqueous supercapacitors provide excellent power density along with extremely long cycle life. [54-55] However, their relatively low energy density has limited their applications in portable devices and long-range electric vehicles. Consequently, the pursuit of higher energy density remains a central focus in the field of supercapacitors.

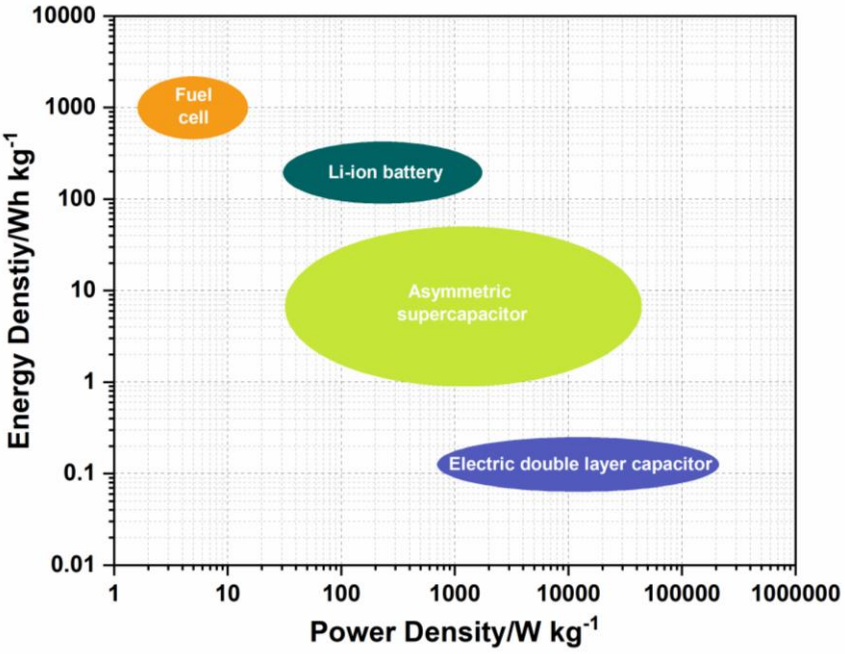

Figure 1.1. *Ragone plot of electrochemical energy storage devices.*

As shown in Figure 1.2, the electrode materials of supercapacitors can be divided into two types according to the energy storage mechanism: electric double-layer capacitors and pseudocapacitors. Following the invention of the first capacitor, the "Leyden jar," by Ewald Georg von Kleist and Pieter van Musschenbroek in the 1700s, capacitors have evolved to encompass various energy storage mechanisms. Despite this evolution, the fundamental structure of capacitors remains consistent, consisting of a cathode where electrons flow in and an anode where electrons flow out. Static electricity can be stored at the interface between a solid electrode and a liquid electrolyte. In 1853, von Helholz built the first electric double-layer model while studying colloidal suspensions.[56] Then, the model was further developed by outstanding electrochemists such as Gouy,[57] Stern,[58] and Grahame,[59] who contributed to the establishment of the modern theory of electric double-layer capacitance (EDLC). Typical EDLC materials, such as activated charcoal,[60-61] graphene,[14-15, 62] and carbon nanotubes,[63] can store more energy than conventional capacitor materials due to their higher specific surface area, nanoscale charge separation distance, and porosity. The charge/discharge process of EDLCs only involves charge rearrangement, which is a physical process. The concept of pseudocapacitor was created in 1971 based on the research involving RuO_2.[64] Pseudocapacitance (PC) is an electricity storage method that relies on the reversible, fast redox reactions occurring at the surface or near-surface area of active materials, accompanied by a change in the valence state of the active materials. Typically, the redox reactions occurring on the oxidized species at the cathode involve the adsorption/desorption of positive charge carriers from the electrolyte.

Organic pseudocapacitive materials comprise a class of substances demonstrating pseudocapacitive behavior in energy storage applications. Typically composed of carbon backbones, these materials have been effectively employed as electrode materials in metal-ion storage systems.[65-66] Owing to the design flexibility,[67-68] low cost,[69-70] and environmental friendliness,[71] organic polymers/small molecules are promising electrode materials for aqueous supercapacitors. However, compared to metal oxide-based electrode materials, organic electrode materials still face challenges related to relatively low energy density.

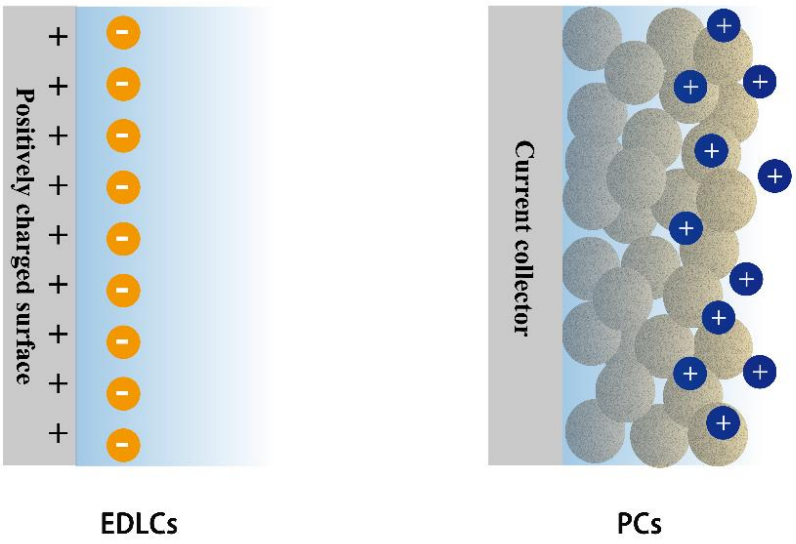

Figure 1.2. *Two types of supercapacitors, including EDLCs and PCs.*

Generally, the energy density of the supercapacitors is determined by the specific capacitance and the cell voltage window according to the equation:

$$E = \frac{1}{2}CV^2 \tag{1.1}$$

The power density of a device can be further determined by:

$$P = E \times \frac{3600}{\Delta t} \tag{1.2}$$

Here, E is energy density, C is the specific capacitance of the supercapacitor, and V is the voltage window of the full-cell device.[72] Thus, broadening the voltage of the full cell is the most straightforward way to improve the energy density of a supercapacitor device. A rational design of the cathodes and anodes allows for an increased potential window, resulting in a device that can deliver more energy.[73-74] However, the potential window of aqueous supercapacitors is limited to 1.23 V by the thermodynamic breakdown potential of water. Developing new electrode material that can widen the potential window beyond this limitation is a promising solution to achieve the goal of higher energy density for aqueous supercapacitors.

1.5. Graphene-based optoelectronic devices

Optoelectronics is a pivotal technology in the information delivery process, and has been seamlessly integrated into consumer electronics markets over the past few decades. Due to its exceptional properties, such as excellent electrical conductivity, ultra-thinness, and high transparency, graphene is considered a promising candidate for applying optoelectronic

materials.[75] Both graphene and functionalized graphene have been used as the electrodes for light-emitting devices.[76-80] Compared to the indium tin oxide (ITO)-based devices, graphene-based optoelectronic devices show excellent device performance as well as outstanding stability, flexibility and reliability. In addition to light-emitting devices, the unique electronic structure of graphene and its derivatives allow them to be promising candidates for solar energy harvesting.[81] It has been proven that graphene can serve as transparent conductive electrode, interfacial layer, and acceptor material.[82-83] Furthermore, multilayer graphene sheets can function as a non-linear optical absorber under nanosecond pulse excitation.[84-85] Graphene-based optical devices including optical modulators, optical polarizers, and optical sensors have been developed by various research groups.[86-88] Functionalized graphene/GO with tunable electronic structures has shown enhanced two-photon absorption behavior, demonstrating a strategy to improve the non-linear optical performance.[89-91] The 2D structure of graphene allows for modification of its electronic properties by chemical functionalization using covalent and noncovalent approaches.[92]

Due to covalent functionalization, the interference of the extended carbon network is inevitable, resulting in notable divergence of the electronic structure.[93] An alternative avenue to achieve the interaction without changing the extended carbon network is the noncovalent approach.[94] Through weak interactions such as electrostatics, π-interaction, hydrogen bonding, and hydrophobic forces, photoactive units can be integrated onto the surface of graphene.

2. Aim

- Design new pyrenetetraone-based derivatives as the graphene-based pseudocapacitive electrode materials for aqueous supercapacitors.
- Investigate the structure-property relationship of the designed materials when used as electrodes in supercapacitors.
- Design a new donor-acceptor molecule and investigate its interactions with graphene.

3. Theory and methodology

3.1. Synthesis of redox-active small molecules and polymers

3.1.1. Reactivity of pyrene

Before discussing the reactivity of pyrene, two different rules should be mentioned: Clar's Rule[95] and Frontier Orbital theory.[96]

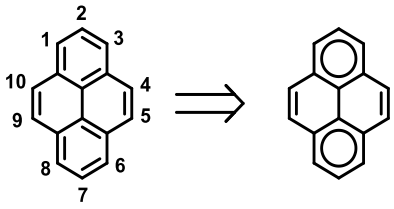

Scheme 3.1. *Model of pyrene according to Clar's rule.*

According to Clar's rule, pyrene is constructed by two full aromatic rings and two annulated double bonds in the K-region (Scheme 3.1). Thus, the K-region of pyrene exhibits an alkene character when reacting with reagents such as OsO_4 and palladium, facilitating the conversion of alkenes into other functional groups.[97-98]

Frontier orbital theory can give the same conclusion as Clar's rule. The highest occupied molecular orbital (HOMO) and the lowest unoccupied molecular orbital (LUMO) of pyrene are shown in Figure 3.1. From the HOMO of the pyrene molecule, higher electron density can be observed at positions 1, 3, 6, and 8, as well as at positions 4, 5, 9, and 10. However, a significant nodal plane passes through positions 2 and 7, making functionalization at these positions more challenging.

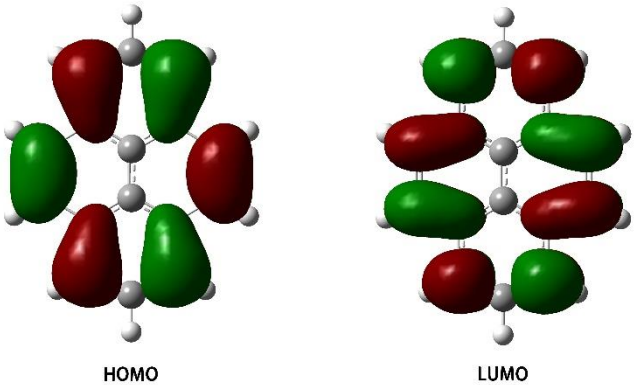

Figure 3.1. *Frontier orbitals of pyrene (HOMO left, LUMO right) calculated by DFT B3LYP (6-31GD).*

3.1.2. Characterization of organic molecules/polymers, graphene, and functionalized graphene

The organic molecules discussed in this thesis are characterized using proton and carbon nuclear magnetic resonance spectroscopy (NMR) as well as infrared spectroscopy (IR) to determine their exact structures. Additionally, the degree of polymerization of the polymers is determined using gel permeation chromatography (GPC). The relative photophysical properties are tested by ultraviolet–visible (UV/Vis) absorption and photoluminescence (PL) spectroscopy. The characterization of graphene and the corresponding nanocomposites is conducted using IR, Raman, UV-Vis absorption, PL, and X-ray photoelectron spectroscopy (XPS).

3.2. Electrochemical test of 2D materials and their nanocomposites

The electrochemical performance of 2D materials and their nanocomposites is evaluated by common testing methods such as cyclic voltammetry (CV), galvanostatic charge/discharge (GCD), and electrochemical impedance spectroscopy (EIS). All of the tests measure three main parameters: potential (V), current (A), and time (s). These measurements are then used to determine capacitance, operating voltage window, equivalent series resistance, energy and power density. Each specific measurement has its own target parameters.

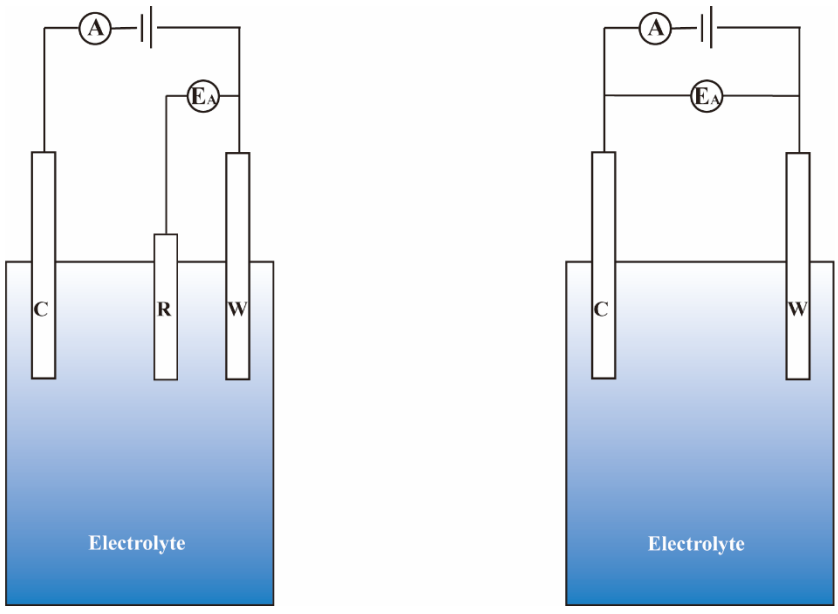

Figure 3.2. *Schematic diagram of 3-electrode setup (left) and 2-electrode setup (right). E_A is the potential applied between reference and working electrodes. W, C, and R are the working, counter, and reference electrodes.*

The potentiostat testing systems in our discussion can be divided into three-electrode systems and two-electrode systems (Figure 3.2). In a three-electrode system, the testing elements

contain a working electrode, a counter electrode, and a reference electrode. The working electrode serves as the testing electrode where the electrochemical transformation of the redox composite takes place. The reference electrode, positioned parallel to the working electrode, measures and controls the potential of the working electrode. It comprises a pair of well-defined redox couples, allowing comparison of the entire electrochemical process between the working electrode and counter electrode. To balance the current passing through the working electrode, a counter electrode is employed, where the opposite electrochemical process occurs. In this thesis, three-electrode systems are utilized to examine the electrochemical performance of the half-cell device, while full-cell devices are tested under the two-electrode system. The working potential is measured between the anode and cathode.

3.2.1. Cyclic voltammetry

During CV measurement, a linearly changing electric potential is applied to the device. The speed of the potential change is called scan rate, which is expressed in mV s^{-1}, and the potential between the working electrode and reference electrode or cathode and anode is called the operating window or potential window. The current in the circuit during the cathodic and anodic sweeps is recorded to analyze the electrochemical process involved in the cycles. In addition, the acquired data are plotted as current (A) *vs.* potential (V).[99]

Using CV measurements with a 3-electrode system is the most suitable method for investigating the charge storage mechanism of a specific electrode material.[100-101] The energy storage mechanism can be evaluated from the shape of the CV curve (Figure 3.3). EDLC-type materials show a symmetric near rectangle shape, which represents an immediate response to the voltage change. The deviation at the corner is the time lag caused by internal resistance during the charge/discharge process. In contrast, battery-type materials exhibit one pair or more than one pair of redox peaks at a certain voltage area, which is an intrinsic property of the material. As mentioned before, the pseudocapacitive material exhibits an energy storage mechanism between EDLC-type and battery-type, which shows a twisted rectangle-shaped CV curve.

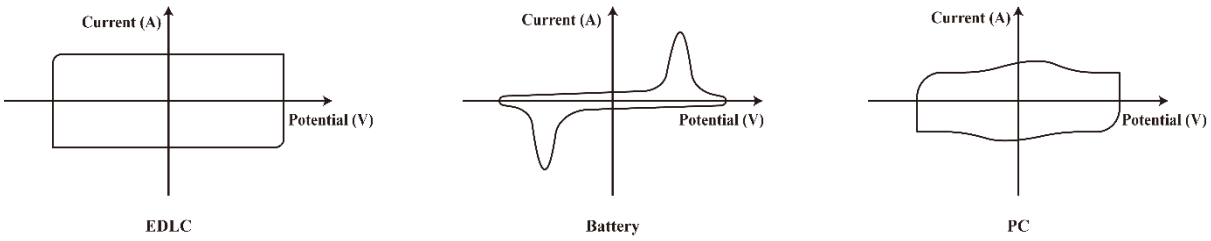

Figure 3.3. *CV curves of the three energy storage mechanisms.*

Besides judging from the shape of a CV curve, kinetic calculations offer a more precise method for distinguishing the charge storage mechanism. In a CV measurement, the electrochemical process can be classified into surface-controlled and diffusion-controlled reactions using the following equation:

$$i = av^b \tag{3.1}$$

Here, v is the scan rate (mV s^{-1}), and i is the corresponding peak current at different scan rates. For a redox reaction controlled by semi-infinite linear diffusion, the current i changes with 0.5 power of scan rate v, indicating battery behavior; if the current i changes linearly with scan rate v, which means b value is 1, the electrochemical process is a surface-controlled, suggesting capacitive behavior.[102]

3.2.2. Galvanostatic charge/discharge (GCD)

Galvanostatic charge/discharge, also known as chronopotentiometry or constant current charge/discharge, is a test in which the material is charged/discharged by a constant current. The potential (V) applied to an electrode is recorded over time (s). The GCD test is considered the most straightforward and accurate way to evaluate the electrochemical performance of supercapacitors. All the vital parameters, such as specific capacitance (C_S), rate performance, operation window, and equivalent series resistance (ESR), can be obtained or derived from the GCD curves. Additionally, the cycling stability can be easily assessed by cyclic GCD test. The energy storage mechanism can also be deduced from the shape of GCD curves.

The capacitance of a supercapacitor is the charge Q stored under a given voltage V, which can be calculated using the following equation:

$$C_T = \frac{Q}{V} \tag{3.2}$$

The specific capacitance is defined as the total capacitance to mass ratio:

$$C_S = \frac{Q}{V \cdot \Pi} \tag{3.3}$$

Here, Π can be the mass, volume, or the area of an electrode material, and the parameter can be converted into the corresponding unit, such as F g^{-1}, F cm^{-3} and F cm^{-2}. Specific capacitance

is one of the most important parameters to evaluate the charge storage ability of an electrode material. Furthermore, total charge can be defined as the product of current and time. The total capacitance in a GCD test can be calculated according to the variation of equation (1) since the current during the test is constant:

$$C_s = \frac{I\Delta t}{V\Pi} \tag{3.4}$$

3.2.3. Electrochemical impedance spectroscopy (EIS)

In a direct current circuit, the obstacle of the current is called resistance. When this concept is extended into alternating current, the resistance is called impedance (Z). In the same testing system, electrochemical impedance spectroscopy measures the impedance of the energy storage device with a low-amplitude alternative voltage. The plotted data is usually expressed in the Bode plot, which consists of log frequency on the X-axis and both the absolute values of the impedance ($|Z|=Z_0$) and the phase-shift on the Y-axis. Another widely used representation is the Nyquist plot, which illustrates impedance at various frequencies.[103-105] EIS can be used to characterize charge transport and mass transport, from which the energy storage mechanism and electrochemical properties can be revealed.[106]

The typical Nyquist plot for supercapacitors is shown in Figure 3.4. The spots on the curve from left to right correspond to the decreasing alternating current frequency. There are several pieces of information worth mentioning in the Nyquist plot. The resistance at point A represents the resistance of the electrode (R_s), including the resistance of the electrode material and the contact resistance between the electrode material and the current collector.[107-108] The diameter of the semicircle between point A and point B is attributed to the charge transfer resistance (R_{CT}), which is the resistance of charge carriers moving across the electrode-electrolyte interface.[109-110] Furthermore, the line BC can be fitted to a straight dash line at intermediate frequencies. The slope of line BC is an important parameter to evaluate the ion diffusion resistance at the electrode-electrolyte interface.[111-112] This thesis also discusses those parameters mentioned above.

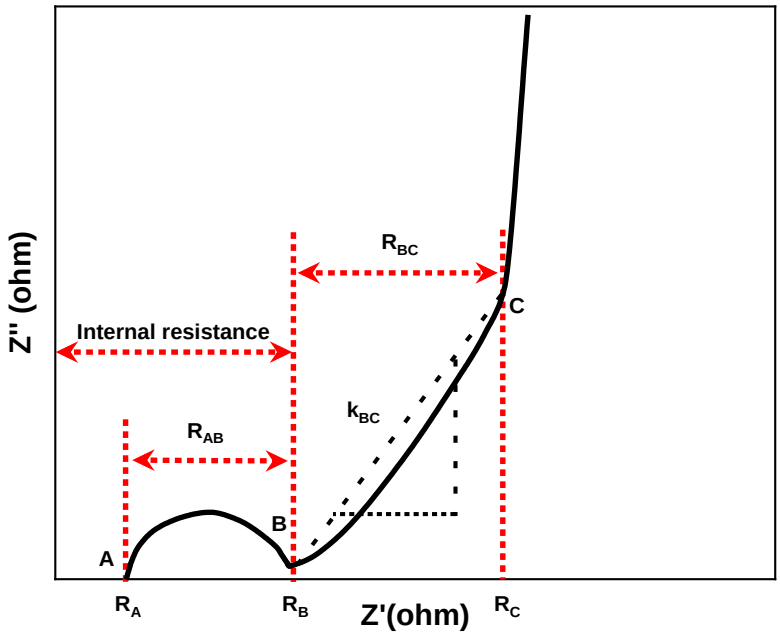

Figure 3.4. *Nyquist plot of a supercapactor.*

3.3. Absorption and emission of synthesized molecules/materials

Spectroscopic characterization techniques are the core toolbox in the research for the photophysical properties of optoelectronic materials. The process usually starts with the absorption of a molecule, which can excite it from ground state to a higher-lying excited state. The absorbance of a sample can be calculated using the Lamber-Beer law:

$$log_{10}\left(\frac{I_0(\lambda)}{I(\lambda)}\right) = A(\lambda) = \varepsilon(\lambda)cl \qquad (3.5)$$

Here, I_0 and I are the intensities of incident light and transmitted light, respectively. A is the absorbance, ε is the molar absorption coefficient, c is the concentration of the solution, and l is the length of the light path through the sample. In addition to providing information on the concentration and presence of different species in a sample, absorption measurements also offer insights into the transition and excitation of a given moiety.

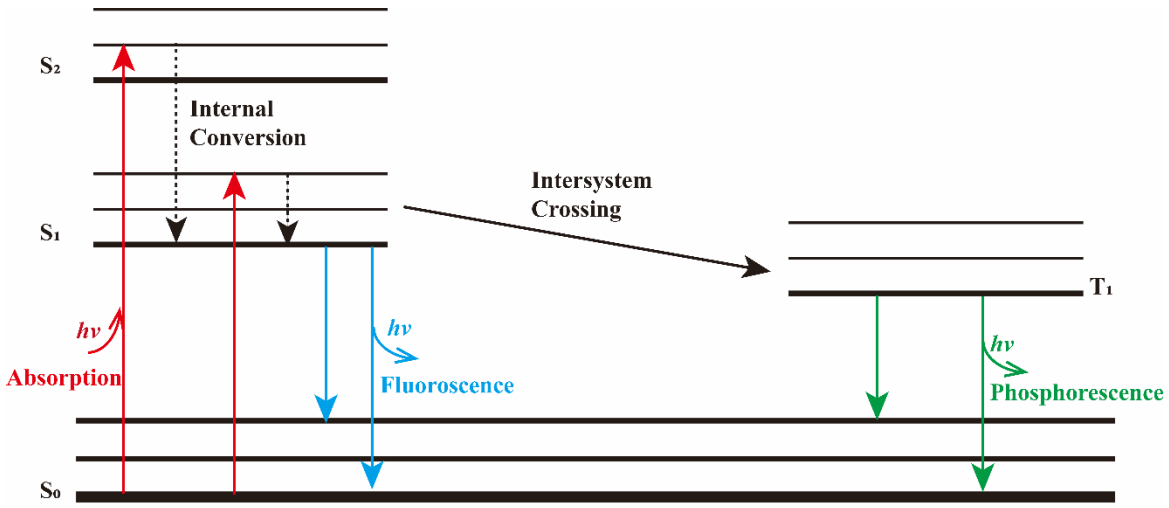

Figure 3.5. *Jablonski diagram showing the mechanism of fluorescence and phosphorescence.*

A fluorophore is excited from the ground state (S_0) to higher excited states (S_1 and S_2) by absorbing photons (Figure 3.5). The molecules usually undergo rapid relaxation (within 10^{-12} seconds) to the lowest vibrational level of S_1, through internal conversion. The return to the vibrational level of the ground state S_0 is responsible for the emissive behavior of a fluorophore. Furthermore, molecules in the S_1 state can also transfer to the excited triplet state T_1. The emission of photons from T_1 to S_0 is known as phosphorescence.

The emission of a molecule can be measured using emission spectroscopy. A suitable excitation wavelength can be selected from the UV/Vis absorption spectra of the molecule. The fluorescence quantum yield can be determined from the absorption and emission spectra of the molecule, using an appropriate reference. Furthermore, interactions between 2D materials and organic molecules/polymers can be investigated by measuring the change in emission intensity.

4. Results and discussion

4.1. PYT and its derivatives as cathodes in supercapacitors

4.1.1. Oxidation of pyrene and its polymerization

Pyrene-4,5,9,10-tetraone (PYT) serves as the pivotal building block for the synthesis of other fused aromatic systems. Also, it can contribute four ketone groups as redox sites in a single molecule, which is a promising candidate for proton storage. Compared to pyrene-4,5-dione, PYT is considered a subsequent K-region (4,5 and 9,10 positions) oxidation product.[113]

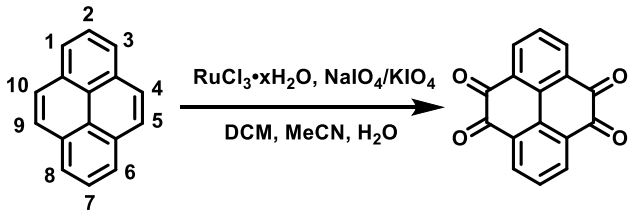

Scheme 4.1. *The oxidation of pyrene.*

To replace the highly toxic osmium tetroxide, a catalytic amount of RuO_4 was generated in situ from the following reaction:

$$8\ Ru^{3+} + 5\ IO_4^- + 12\ H_2O \rightarrow 8\ RuO_4 + 5\ I^- + 24\ H^+$$

The optimized reaction condition is shown in the following table:

Table 4.1. *Optimized reaction condition for the oxidation of pyrene.*

Entry	Oxidant	T/°C	Time/h	Yield
1	$NaIO_4$	25/35	16/3	----------
2	$NaIO_4$	25/35	24/3	11%
3	$NaIO_4$	25/35/40	8/2/1	13%
4	KIO_4	25/30/35/40/50	5.5/1/2/3/4	9%
5	KIO_4	50	8h	21.3%
6	$NaIO_4$	0/35/40	6/2/1	----------
7	KIO_4/$NaIO_4$	50	8h/3h	**30%**
8	KIO_4	70	5h	15%

The oxidation is controlled by adjusting the solubility of the oxidant. Sodium periodate shows excellent aqueous solubility (30.4 g/100 ml) at 40 ℃, which is 30 times greater than that of the corresponding potassium salt (1.0 g/100 ml).

Linear polymer molecules that contain nitrogens have been studied as electrode materials such as polypyrrole,[114] polyanaline[115-117], and polyindole.[118] Due to the irreversible redox reaction and the swelling of the electrode during the charge/discharge process, the cycle life of those conducting polymer electrodes are restricted.[119-120] Introducing heteroaromatic structures can significantly increase the chemical stability of the redox sites.[121]

The aromatic-fused redox polymers are synthesized by condensation reactions between pyrenetetraone and amines. Three different types of polymer units are designed to investigate the electrochemical performance of the aromatic C=N species in different structures. Based on the different amine structures (Scheme 4.2), the polymers are synthesized with the names as PPYT, PPYTQ, and tPPYT. If the PPYT polymer is set as the reference sample among the three polymers, the PPYTQ polymer has introduced 2 additional ketone groups as redox sites in a single polymer unit, potentially resulting in greater pseudocapacitive contributions. In addition, the tPPYT polymer with a sigma bond as the rotating shaft is also designed. Due to the existence of hydrogen in the ortho position of the 4,4'-sigma bond, the entire polymer shows a twisted structure with a dihedral angle between adjacent polymer units. Compared to the other two planar polymers, the twisted structure may prevent the tPPYT polymer from interacting with graphene, leading to lower electrochemical performance.

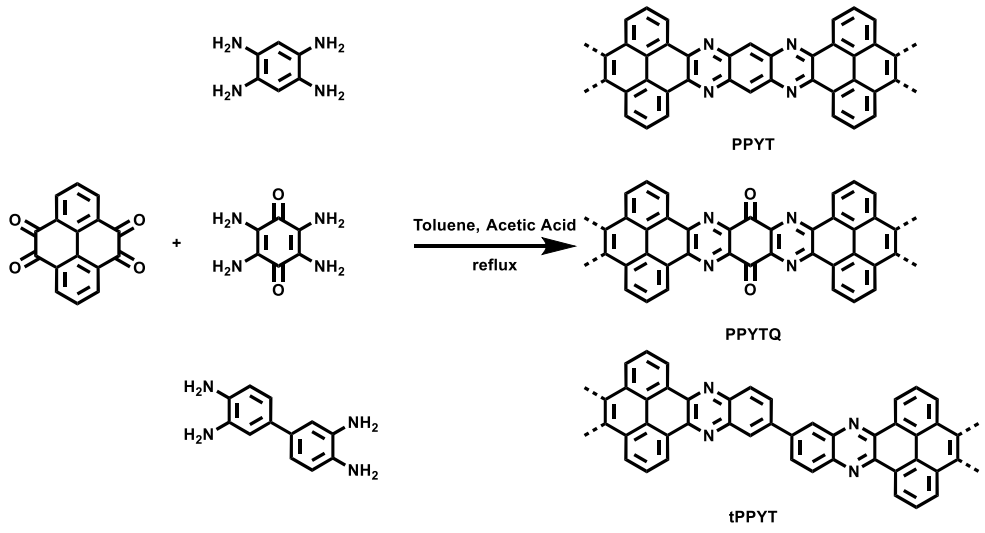

Scheme 4.2. *Synthetic route of the three polymers including PPYT, PPYTQ, and tPPYT.*

4.1.2. Characterization of PYT-based nanocomposites

In the present study, two different kinds of commercially available rGO are used as the conducting matrix for the nanocomposites. The rGO from Graphenea (GN) has a much higher oxygen content, compared to the one from LayerOne (LO).

The interaction between the PYT and rGO is investigated by Fourier-transform infrared spectroscopy (Figure 4.1). The number in the sample name corresponds to the weight ratio between the PYT and rGO. The pristine GN and LO graphene don't show any significant absorption peak in the range of 2200 cm^{-1} to 650 cm^{-1}. With the existence of the four ketone groups, PYT shows a strong absorption band at 1674 cm^{-1}. The band at 1273 cm^{-1} can be attributed to the bending of the C-H bonds. Both bands have shifted to lower wavenumbers after the PYT molecule was combined with rGO due to π-π interactions. It is worth mentioning that the absorption intensity of the PYT/LO 4-5 nanocomposite is lower than that of the PYT/GN 4-5 nanocomposite. The absorption peaks even disappeared in the PYT/LO 2-7 nanocomposite. This phenomenon may be caused by the vibrational confinement of the PYT molecules induced by the graphene nanosheets.

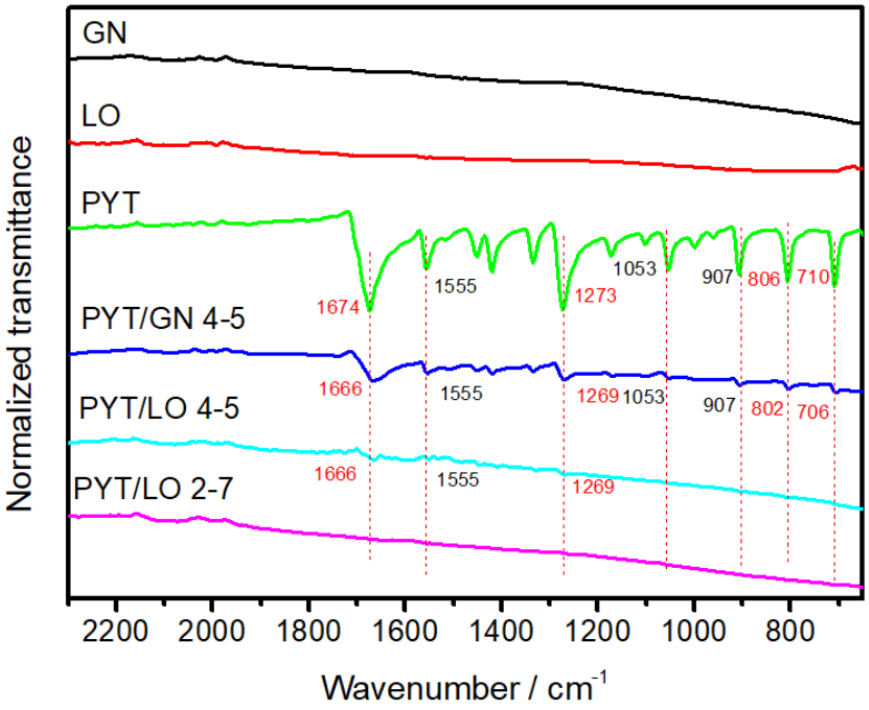

Figure 4.1. *FT-IR spectra of PYT, GN, LO, and the corresponding nanocomposites.*[122]

The elemental content of the composite is further investigated by X-ray photoelectron spectroscopy (Figure 4.2). The elemental content is shown in Table 4.2. The PYT molecule shows an oxygen content of 18.1% due to the existence of the four carbonyl groups. Compared

to the LO, the GN shows a higher oxygen content (≈ 530 eV), indicating a lower degree of reduction. For the nanocomposite electrodes, all the elemental content is in line with the theoretical values.

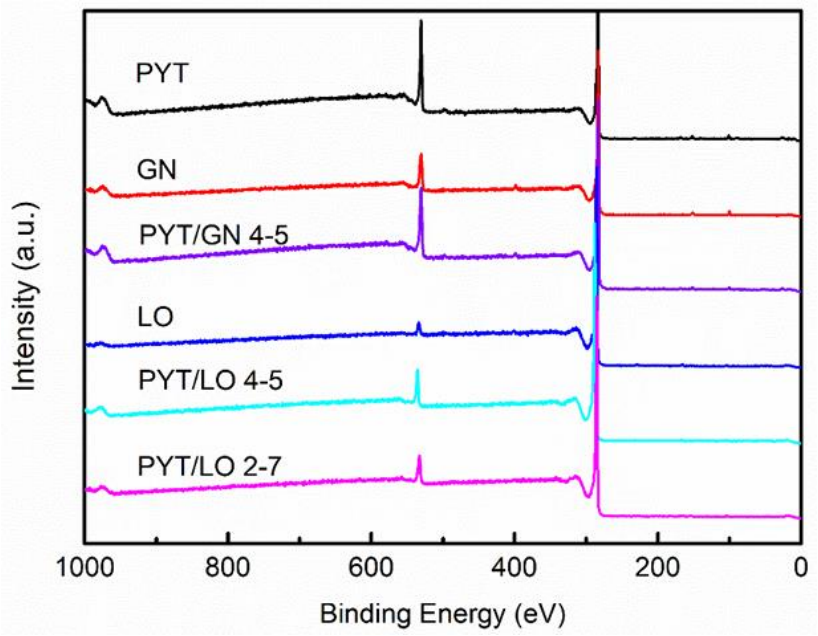

Figure 4.2. *Survey scan curves of PYT, GN, LO graphene, and the corresponding nanocomposites.*[122]

Table 4.2. *Elemental content of PYT and the as-obtained nanocomposites.*

Sample	C (%)	O (%)
PYT	81.9	18.1
GN	88.2	11.8
PYT/GN 4-5	84.8	15.2
LO	96.8	3.2
PYT/LO 4-5	93.6	6.4
PYT/LO 2-7	94.5	5.5

4.1.3. Characterization of PPYT, PPYTQ, tPPYT and the corresponding nanocomposites

The degree of polymerization of the three polymers was measured by GPC. The PPYT polymer exhibits an average molecular weight (M_W) of 39277 Daltons, while the M_W of the PPYTQ

polymer is 43906 Daltons. Unfortunately, due to the poor solubility of the tPPYT polymer in common solvents used for GPC measurements, the analysis cannot be performed.

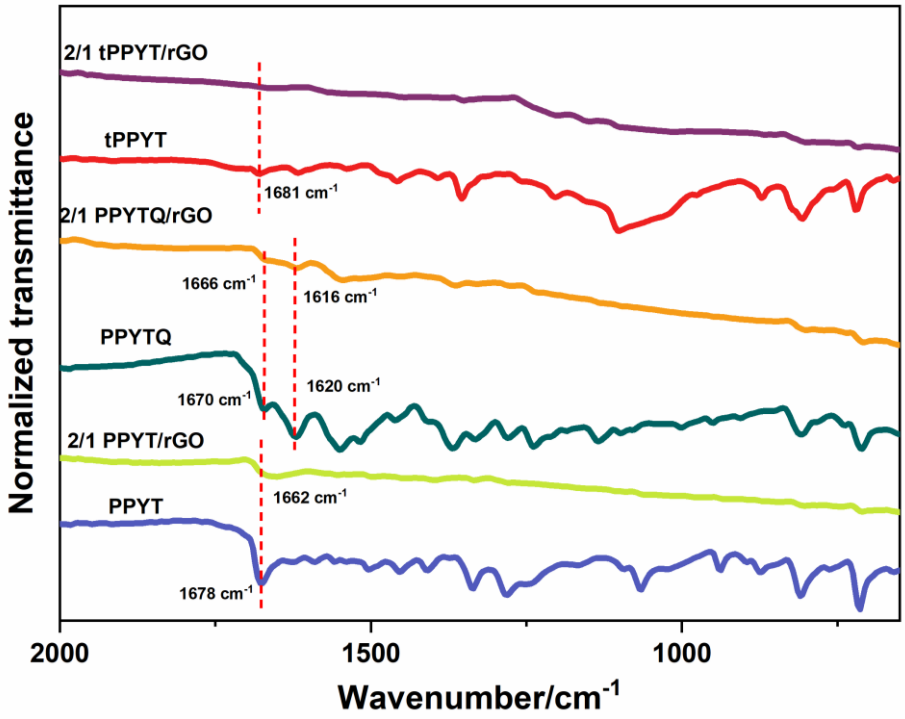

Figure 4.3. *FTIR spectra of PPYT, PPYTQ, tPPYT, and the corresponding nanocomposites.*[123]

The interaction between the three polymers and rGO is studied by UV/Vis absorption and FT-IR spectroscopy (Figure 4.3). The absorption bands for the stretching vibration of the C=N double bond can be found at around 1678 cm^{-1} for the PPYT polymer. Similar peaks can be seen at 1670 cm^{-1} and 1681 cm^{-1} for the PPYTQ and tPPYT polymers, respectively. For comparison, the corresponding peak of the 2/1 PPYT/rGO nanocomposite moves to a lower frequency with a shift of 16 cm^{-1}, indicating the interaction between the PPYT and rGO. A similar 4 cm^{-1} shift can also be found in the spectrum of the 2/1 PPYTQ/rGO nanocomposite. However, for the 2/1 tPPYT/rGO nanocomposite, no significant absorption peak can be found in its IR spectrum.

UV/Vis spectrophotometric titration was deployed to further investigate the interaction between the conducting polymers and rGO (Figure 4.4). The UV/Vis spectrum of rGO was measured in ethanol as the reference material. Due to the π–π^* transitions of the C=C double bonds, the rGO shows an absorption band at 271nm. As for the PPYT polymer, a strong absorption band at 323 nm and two less intensitive bands at 426 nm and 490 nm can be

observed. With the increase of the concentration of the rGO, the absorption band at 323 nm shows a 2 nm redshift after baseline correction, indicating that there is an interaction between the PPYT and rGO (Figure 4.4a). Besides, the same trend is also observed during the titration between the PPYTQ and rGO. A 5 nm redshift from 539 nm to 544 nm is found when the PPYTQ/rGO ratio reaches 4:1, while the other band remains unchanged (Figure 4.4b). In contrast, no shift is observed during the titration between the tPPYT and rGO (Figure 4.4c). The difference is caused by the different conformations of the three polymers on the rGO in ethanol. The planar structure of the PPYT and PPYTQ allows them to interact readily with the rGO matrix, while the tPPYT requires preorganization before attaching onto the rGO, because of the dihedral angle between the flat polymer units.

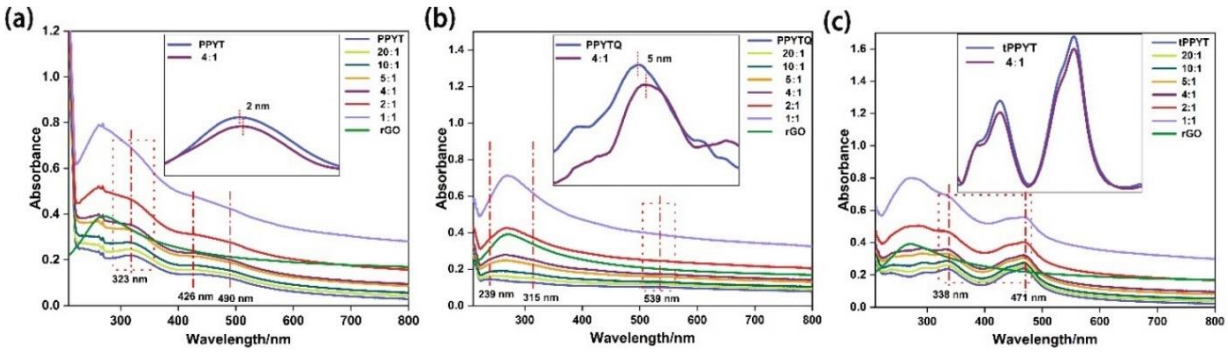

Figure 4.4. *UV-Vis absorption spectra of a titration between 0.1 mg/ml of rGO and 0.01 mg/ml of (a) PPYT, (b) PPYTQ, and (c) tPPYT in ethanol. The ratio shown in the legend is polymer/rGO.*[123]

The elemental content of the nanocomposite is further determined using XPS (Figure 4.5), and the composition is listed in Table 4.3. All the samples show the major peaks of C1s and O1s. Besides, N1s peaks can also be found due to the existence of the pyrazine groups.

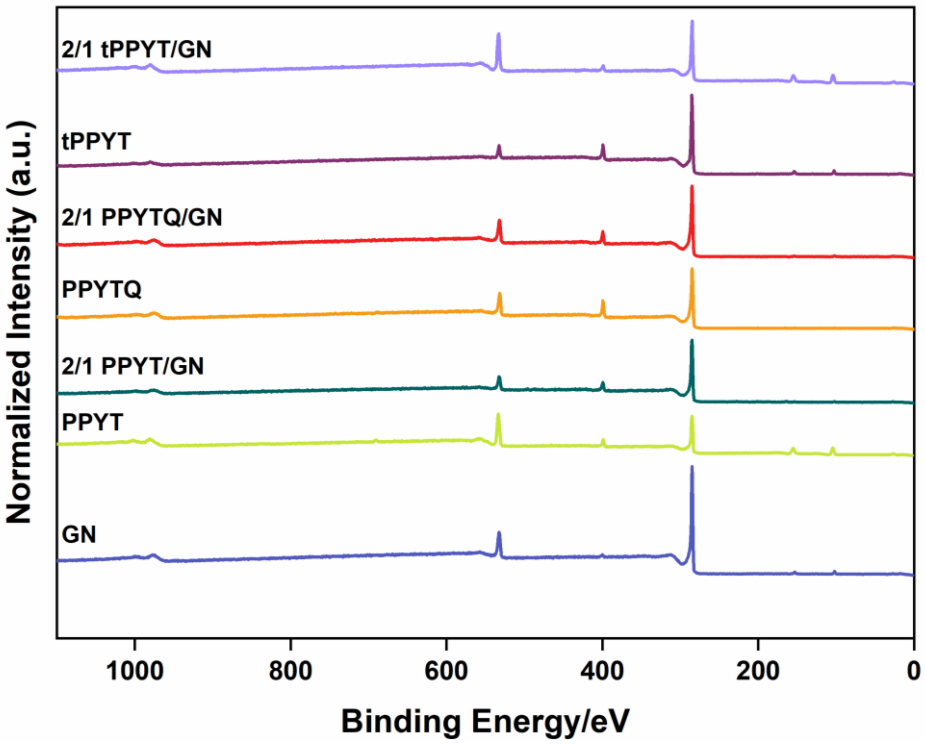

Figure 4.5. *Broad survey spectra of all the three polymers and the corresponding nanocomposites.*[123]

Table 4.3. *The elemental content of all the polymers and nanocomposites.*

Materials	C (%)	O (%)	N (%)
rGO	88.2	11.8	0
PPYT	80.0	13.0	7.0
2/1 PPYT/rGO	84.3	8.9	6.8
PPYTQ	75.5	13.0	11.5
2/1 PPYTQ	78.0	13.6	8.4
tPPYT	80.5	11.7	7.8
2/1 tPPYT/rGO	77.8	15.7	6.5

It is worth mentioning that the high-resolution N1s spectra can be deconvoluted into two significant peaks at 399.6 eV for the pyrazine nitrogen and 400.7 eV for the protonated nitrogen (Figure 4.6). Compared with the PPYT and tPPYT polymers, the PPYTQ polymer shows a relatively lower protonation ratio (14.5%) since the adjacent carbonyl groups decrease the electron density of the nitrogen, leading to a lower proton affinity.

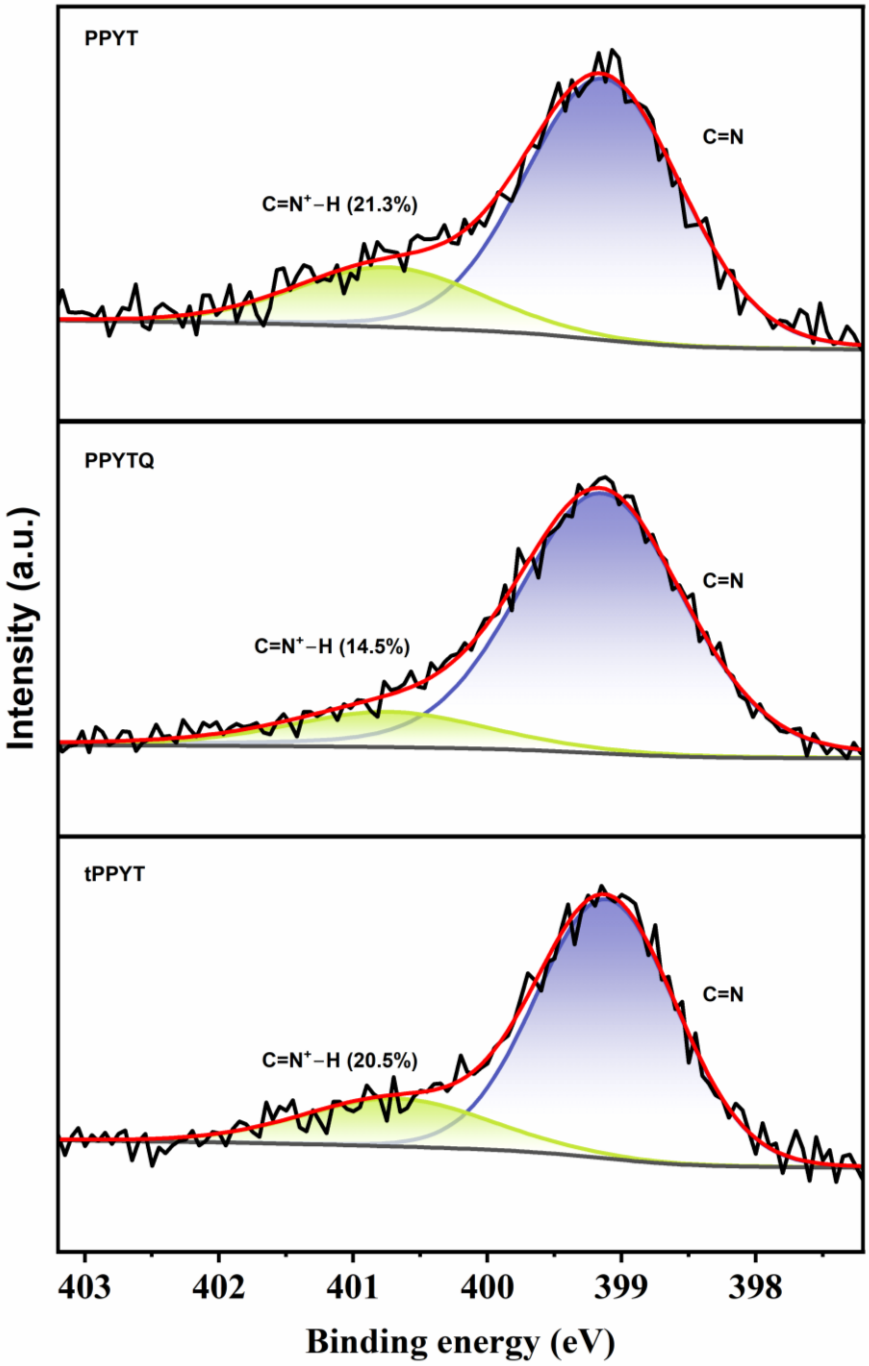

Figure 4.6. *N1s spectra of the PPYT, PPYTQ, and tPPYT polymers.*[123]

4.1.4. Electrochemical measurement of PYT as the cathode

The electrochemical measurement of PYT was performed in a three-electrode system in a 1 M H_2SO_4 electrolyte with Ag/AgCl as the reference electrode.

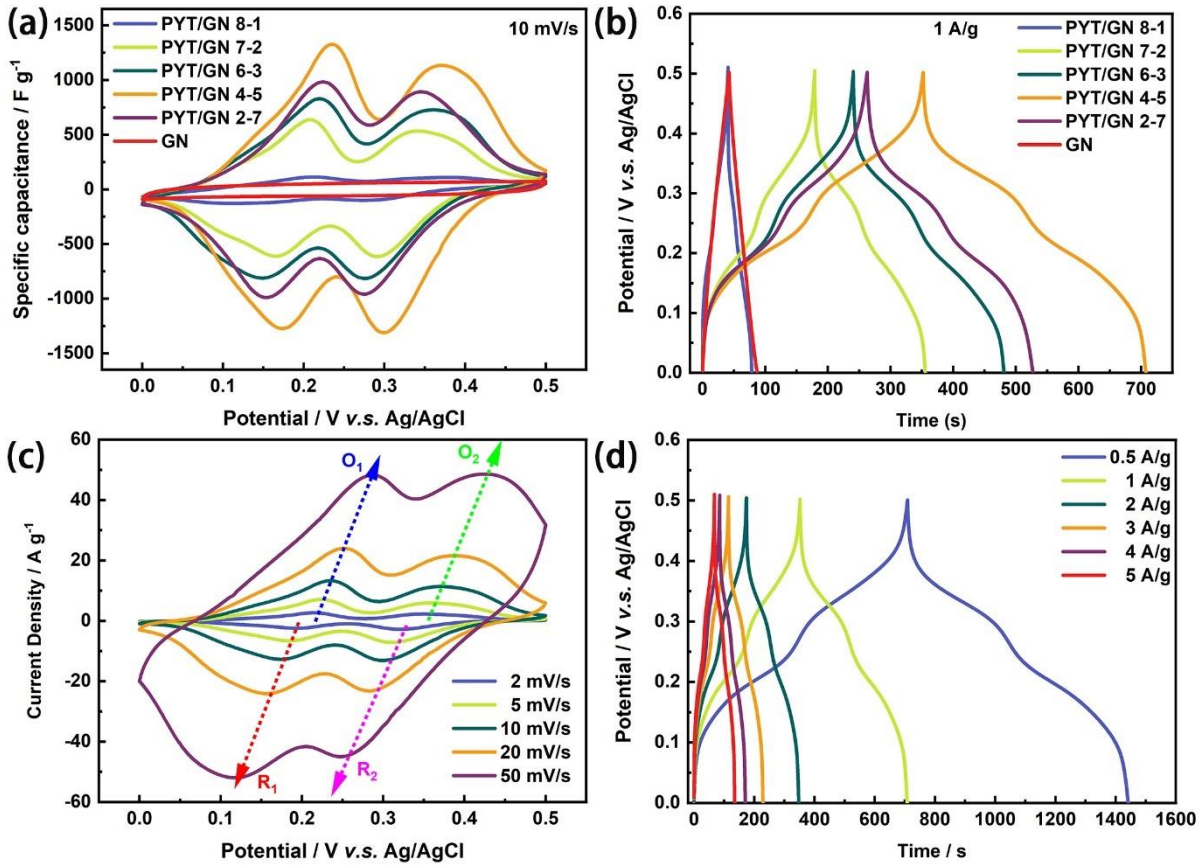

Figure 4.7. *Electrochemical characterization of PYT with GN in a three-electrode system. (a) CV curves of the PYT/GN nanocomposites with different ratios at a scan rate of 10 mV s^{-1} (b) GCD curves of the PYT/GN nanocomposites with different ratios at a current density of 1 A g^{-1}. (c) CV curves of the PYT/GN 4-5 nanocomposite at different scan rates. (d) GCD curves of the PYT/GN 4-5 nanocomposite at different current densities.*[122]

All the CV curves of different nanocomposites with various PYT/GN ratios are shown in Figure 4.7a. The CV curve of GN shows a rectangular shape, indicating the electrical double-layer capacitive behavior. After adding the PYT molecule, the nanocomposites show two pairs of redox peaks at ~ 0.17/0.23 and ~ 0.30/0.37 (*v.s.* Ag/AgCl), which can be attributed to the redox reactions of the four carbonyl groups. Among the various ratios, the PYT/GN 4-5 nanocomposite can circle the largest area after normalization, indicating the highest specific capacity. Figure 4.7b shows the constant current charge/discharge curves of all the ratios at 1 A g^{-1}. The GN electrode exhibits a triangle-shaped GCD curve, while the other nanocomposites exhibit redox plateaus due to the presence of the PYT molecule. With the optimized ratio in hand, the electrochemical performance of the PYT/GN 4-5 electrode is further investigated at different scan rates and various current densities (Figure 4.7c and d). With the increase of the scan rate, the redox peaks shifted to more positive and negative sides, which can be ascribed to the internal resistance. Even at a scan rate of 50 mV s^{-1}, the nanocomposite can still retain

its shape, indicating good electrochemical reversibility. Moreover, the PYT/GN 4-5 electrode exhibits excellent specific capacitance of 733, 711, 695, 686, 679, and 673 F g^{-1} at 0.5-5 A g^{-1} under constant current charge/discharge.

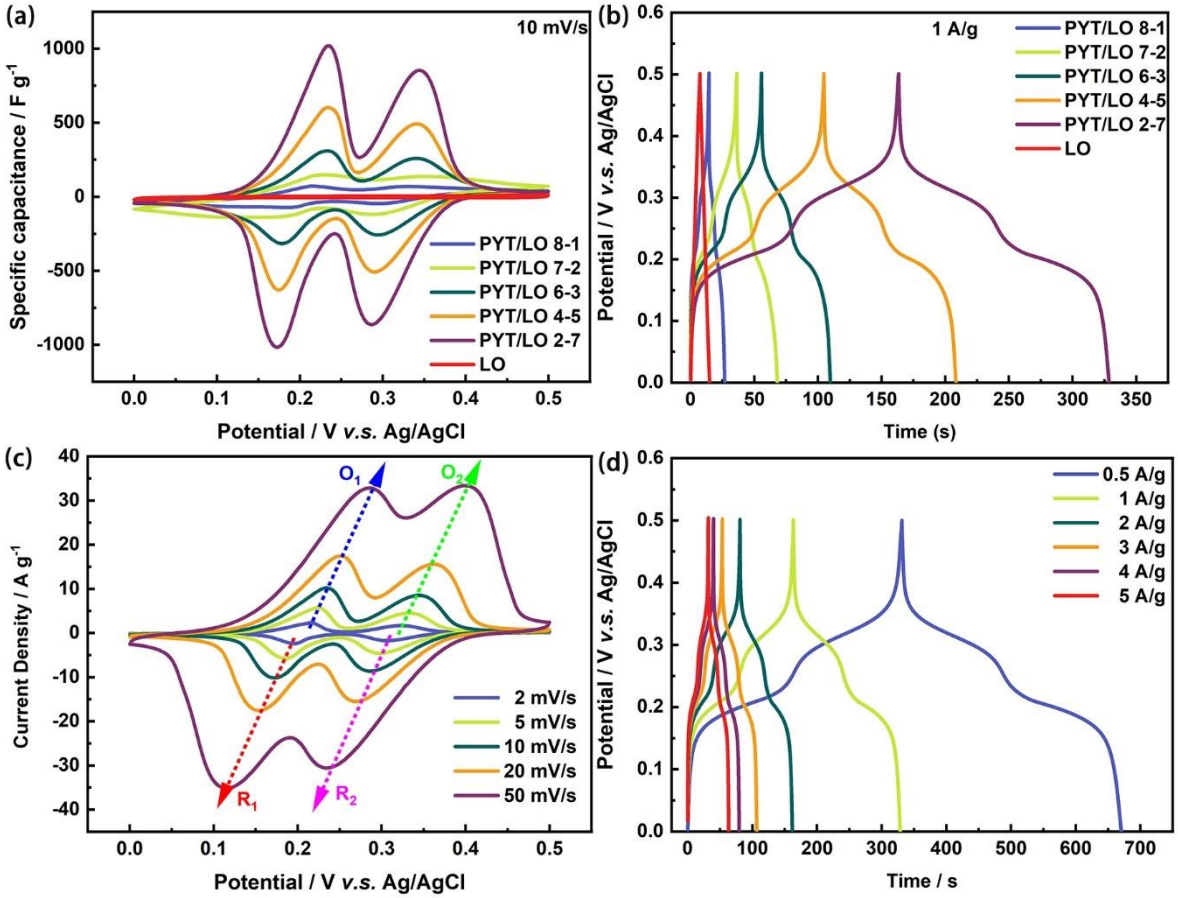

Figure 4.8. *Electrochemical characterization of PYT with LO in a three-electrode system. (a) CV curves of the PYT/LO nanocomposites with different ratios at a scan rate of 10 mV s^{-1} (b) GCD curves of the PYT/LO nanocomposites at different ratios at 1 A g^{-1}. (c) CV curves of the PYT/LO 2-7 nanocomposite at different scan rates. (d) GCD curves of the PYT/LO 2-7 nanocomposite at different current densities.*[122]

The same measurement is applied to the PYT/LO nanocomposites (Figure 4.8). However, they show a different trend compared to the PYT/GN nanocomposites. When the percentage of PYT is 20%, the nanocomposite can reach the highest specific capacitance (Figure 4.8a and b), while the one for the PYT/GN nanocomposites is 40%. The replacement of GN with LO does not alter the position of the redox peaks (Figure 4.8c). Moreover, the PYT/LO nanocomposite exhibits a lower specific capacitance of 339, 331, 324, 320, 318, and 316 F g^{-1} at 0.5–5 A g^{-1} (Figure 4.8d).

The energy storage mechanism is evaluated based on equation 3.1. The b value of the PYT/GN 4-5 and PYT/LO 2-7 nanocomposites is deduced from Figure 4.9. The b values of the four

redox peaks for the PYT/GN 4-5 are 0.90, 0.95, 0.95, and 0.86, which are in the range of 0.5 to 1, indicating that the surface-controlled reaction dominates the charge/discharge process. The b values of the PYT/LO 2-7 electrode are 0.82, 0.92, 0.82, and 0.89, similar to the ones of the PYT/GN 4-5 nanocomposite.

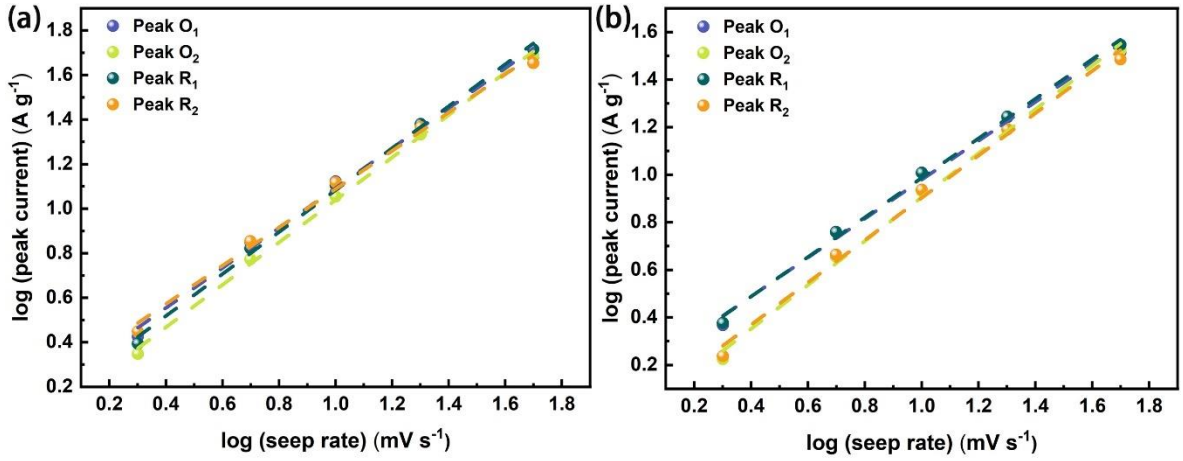

Figure 4.9. *(a) log(i) vs log(v) plots according to the CV curves of the PYT/GN 4-5 nanocomposite. (b) log(i) vs log(v) plots according to the CV curves of the PYT/LO 2-7 nanocomposite.*[122]

Electrochemical impedance spectroscopy (EIS) is deployed to further understand the energy storage mechanism of the GN, LO, PYT/GN 4-5, and PYT/LO 2-7 (Figure 4.10). In the low-frequency region, all the electrodes exhibit nearly vertical lines, indicating low proton diffusion impedance. The fitted result for the high-frequency region exhibits the internal resistance of the electrode and the charge-transfer resistance (Table 4.4). Interestingly, the PYT/rGO nanocomposite electrodes show a lower charge-transfer resistance than the pure GN and LO electrodes, which can be ascribed to the increased wettability of the nanocomposite electrodes.

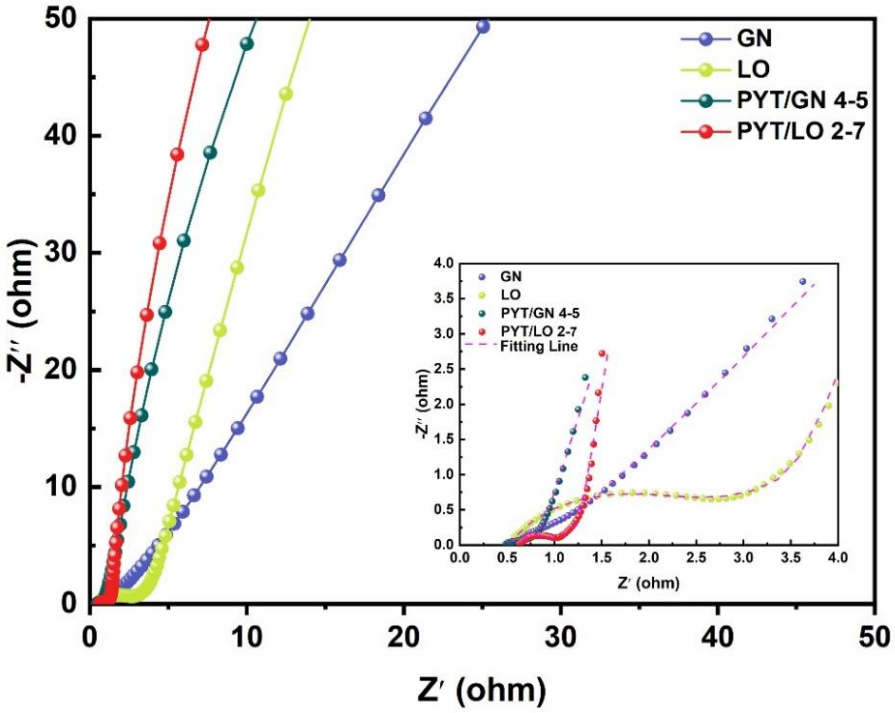

Figure 4.10. *Nyquist plots of EIS for the GN, LO, PYT/GN 4-5 and PYT/LO 2-7.*[122]

Table 4.4. *Impedance parameters simulated from the equivalent circuits.*

Sample	Rs	R_{CT}
GN	0.51	0.96
LO	0.53	1.99
PYT/GN 4-5	0.49	0.15
PYT/LO 2-7	0.66	0.28

4.1.5. Electrochemical test of the polymer/rGO nanocomposites

The electrochemical performance of the PPYT/rGO nanocomposite electrodes is measured by a three-electrode in 1M sulfuric acid electrolyte (Figure 4.11). The normalized CV curve of the rGO electrode shows a rectangular-shaped CV curve, indicating its EDLC behavior (Figure 4.11a). Combining PPYT and rGO to form the nanocomposite electrodes introduces a pair of redox peaks at ≈ 0.38 V/0.18 V (vs Ag/AgCl). In contrast to small organic molecules, when conducting polymers constitute the majority of the nanocomposite, the electrode demonstrates enhanced specific capacitance. Among all the ratios, the CV curve of the 2/1 PPYT/rGO electrode endows the largest area, implying the best electrochemical performance. However, for the 3/1 PPYT/rGO electrode, it showed a lower specific capacitance, possibly due to the

relatively low conductivity. The same trend can be found in the GCD curves at a current density of 1 A g^{-1} (Figure 4.11b). The redox plateaus can be found at the corresponding potentials of the redox peaks in the CV curves. With the contribution of the plateaus, the 2/1 PPYT/rGO electrode can exhibit the highest specific capacitance due to the longest charge/discharge time among all the nanocomposites. The CV of the optimized electrode is measured at various scan rates from 2-50 mV s^{-1}(Figure 4.11c). The shape of the CV curves is conserved at different scan rates, indicating good electrochemical stability and reversibility. In addition, the specific capacitance of the 2/1 PPYT/rGO electrode is measured using the GCD measurement (Figure 4.11d). The specific capacitance of the nanocomposites at different ratios is displayed in Figure 11e. The 2/1 PPYT/rGO nanocomposite can exhibit the highest specific capacitance of 591, 550, 533, 520, and 508 F g^{-1} at 1–5 A g^{-1}, respectively. It is notable that the 2/1 PPYT/rGO nanocomposite demonstrates an 86% retention at a current density of 5 A g^{-1}. Due to the limited electrical conductivity, the 3/1 PPYT/rGO electrode shows a lower specific capacitance and the poorest rate performance (Figure 4.11e). Moreover, the b values of the 2/1 PPYT/rGO electrode are 0.68 and 0.64, which are close to 0.5, indicating that the charge/discharge process is predominantly diffusion-controlled (Figure 4.11f).

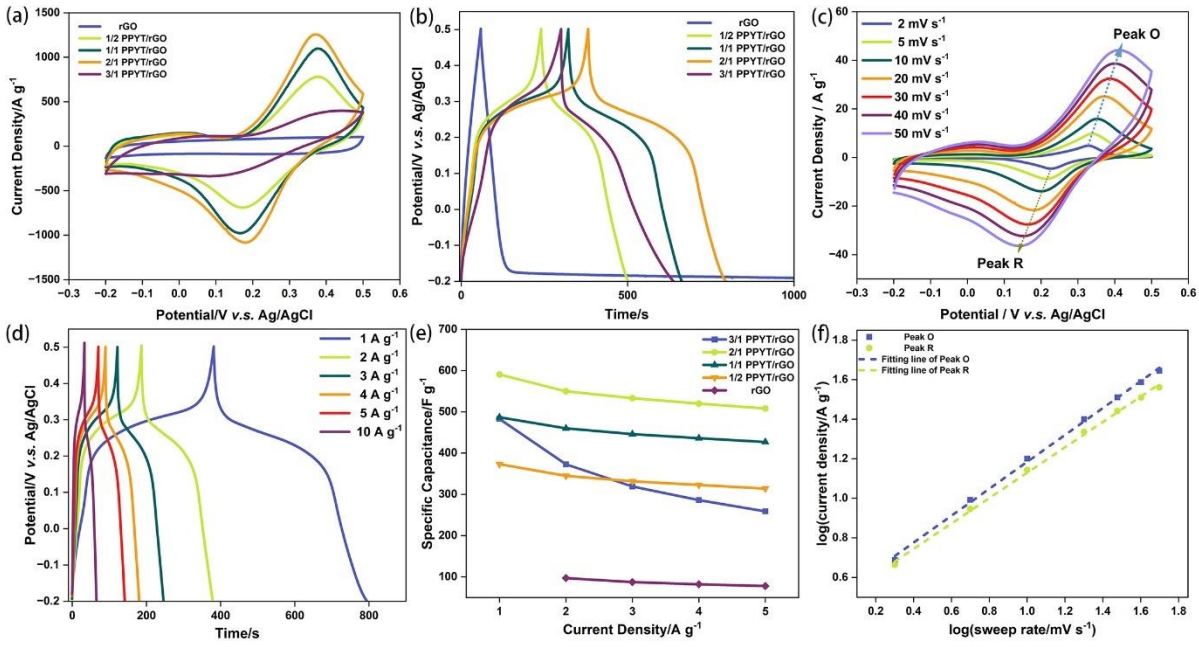

Figure 4.11. *Electrochemical characterization of the PPYT/rGO electrodes at different ratios in a three-electrode system. (a) CV curves of the rGO and PPYT/rGO electrodes at 20 mV s^{-1}. (b) GCD curves of the rGO and PPYT/rGO electrodes at 1 A g^{-1}. (c) CV curves of the 2/1 PPYT/rGO electrode at different scan rates. (d) GCD curves at various current densities. (e) The specific capacitance of the rGO and PPYT/rGO electrodes at different current densities. (f) log(i) vs log(v) plots according to the CV curves.*[123]

A similar scenario can also be observed in the case of PPYTQ (Figure 4.12). Compared to the PPYT polymer, PPYTQ shows two pairs of redox peaks due to the existence of the carbonyl groups. From the CV curves and GCD curves of the nanocomposite electrodes at different ratios (Figure 4.12a and b), th 2/1 PPYTQ/rGO nanocomposite shows the best electrochemical performance among all the ratios. Under various scan rates, the 2/1 PPYTQ/rGO electrode can retain almost the same shape in the CV curves, indicating good reversibility (Figure 4.12c). The 2/1 PPYTQ/rGO electrode exhibits specific capacitances of 603, 511, 470, 447, and 418 F g^{-1} at current densities of 1–5 A g^{-1} (Figure 4.12d). However, compared to the 2/1 PPYT/rGO electrode, it shows lower rate performance, with a decrease to 69% at 5 A g^{-1} compared to 1 A g^{-1}. As the PPYTQ polymer content decreases, the nanocomposite electrodes exhibit improved rate performance owing to the reduced pseudocapacitive contribution during the charge/discharge process (Figure 4.12e). It is worth mentioning that the 3/1 PPYTQ/rGO electrode shows a similar attenuation rate compared to the 2/1 PPYTQ/rGO electrode, especially at high current density. The b values of the four redox peaks are 0.79, 0.78, 0.78, and 0.84, indicating that both diffusion-controlled and surface-controlled reactions exist in the charge storage mechanism (Figure 4.12f).

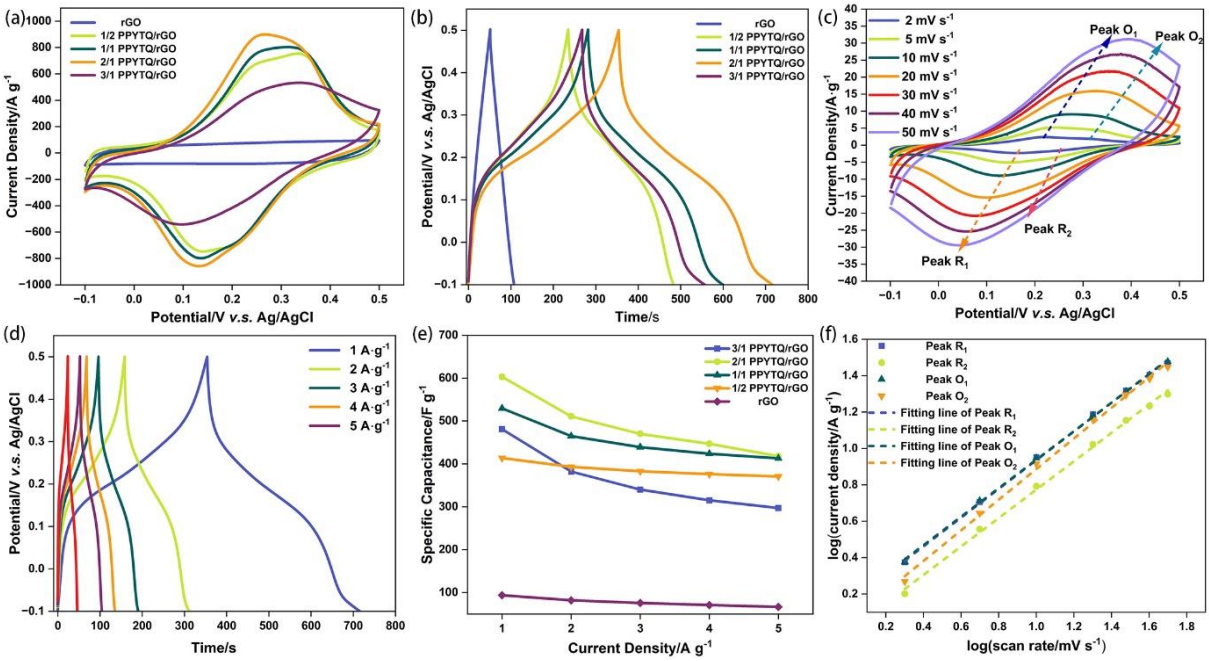

Figure 4.12. *Electrochemical characterization of the rGO and PPYTQ/rGO electrodes at different ratios in a three-electrode system. (a) CV curves of the rGO and PPYTQ/rGO electrodes at 20 mV s^{-1}. (b) GCD curves of the rGO and PPYTQ/rGO electrodes at 1 A g^{-1}. (c) CV curves of the 2/1 PPYTQ/rGO electrode at different scan rates. (d) GCD curves of the rGO and PPYTQ/rGO electrodes at different current densities. (e) The specific capacitance*

of the rGO and PPYTQ/rGO electrodes at different current densities. (f) log(i) v.s. log (v) plots according to the CV curves.[123]

Then the electrochemical performance of the tPPYT polymer is also tested and it shows a fairly poor performance compared to the other two polymers (Figure 4.13). The 2/1 tPPYT/rGO electrode shows a very narrow potential window and a large number of electrode side reactions during the charging and discharging processes.

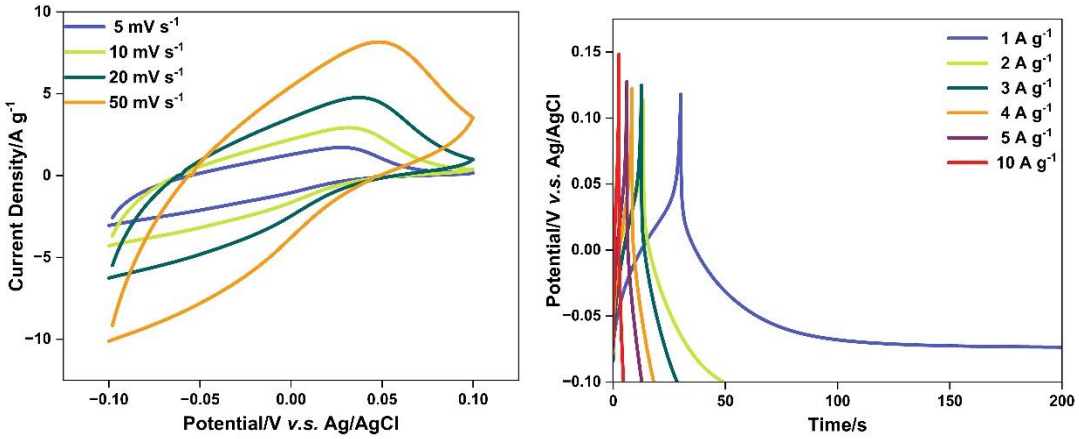

Figure 4.13. *Electrochemical characterization of the 2/1 tPPYT/rGO electrodes in a three-electrode system.*[123]

Figure 4.14 is the Nyquist plot of the rGO and nanocomposite electrodes. The vertical line in the low-frequency region suggests the low proton diffusion impedance and capacitive behavior. Similar to the PYT/graphene nanocomposite electrodes, the polymer/rGO nanocomposite electrodes show a lower charge-transfer resistance compared to the rGO electrode (Table 4.5).

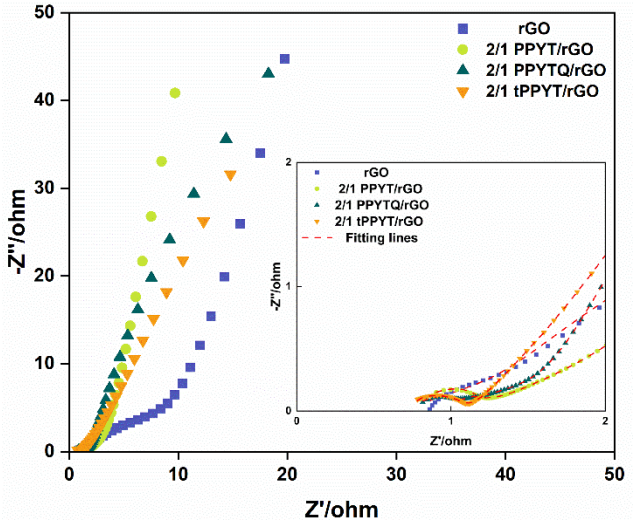

Figure 4.14. *Nyquist plots of EIS for the rGO, 2/1 PPYT/rGO, 2/1 PPYTQ/rGO, and 2/1 tPPYT/rGO.*[123]

Table 4.5. *Impedance parameters simulated from the equivalent circuits.*

Sample	Rs (ohm)	Rct (ohm)
rGO	0.73	1.13
2/1 PPYT/rGO	0.82	0.32
2/1 PPYTQ/rGO	0.81	0.21
2/1 tPPYT/rGO	0.83	0.45

4.1.6. Electrochemical test of the asymmetric supercapacitors

With the promising cathodes in hand, annealed $Ti_3C_2T_x$ (A-$Ti_3C_2T_x$) is chosen as the anode material. The calcination process can remove the electrochemical inert groups, such as F, from the surface of the $Ti_3C_2T_x$. After the treatment, the anode can exhibit a specific capacitance of 508 F g^{-1} at 2 A g^{-1}. The mass loading ratio of the cathode and anode is calculated based on the equation below:

$$\frac{m^+}{m^-} = \frac{C^- V^-}{C^+ V^+} \tag{4.1}$$

The assembled devices are further investigated by CV and GCD. The ASC is named as PYT/GN 4-5//A-$Ti_3C_2T_x$. The potential window of the full device is further determined by CV measurement at 50 mV s^{-1} (Figure 4.15a). At 1.5 V, the CV curve shows a sharp peak, which can be attributed to the evolution of oxygen[124]. Due to the proton-coupled electron exchange within the cathode and anode, the CV curves show obvious redox behavior (Figure 4.15b). Moreover, the CV curves can maintain a similar shape under different scan rates, indicating good chemical stability and reversibility. The device shows a specific capacitance (Figure 4.15c) of 63.6, 60.9, 58.6, 56.8, and 48.6 F g^{-1} at 1–10 A g^{-1}, respectively. Additionally, the device can still possess a specific capacitance retention of 91.4% after 5000 charge/discharge cycles (Figure 4.15d). Based on equations 1.1 and 1.2, the device can convey an energy density of 18.4 Wh kg^{-1} at a power density of 700 W kg^{-1}.

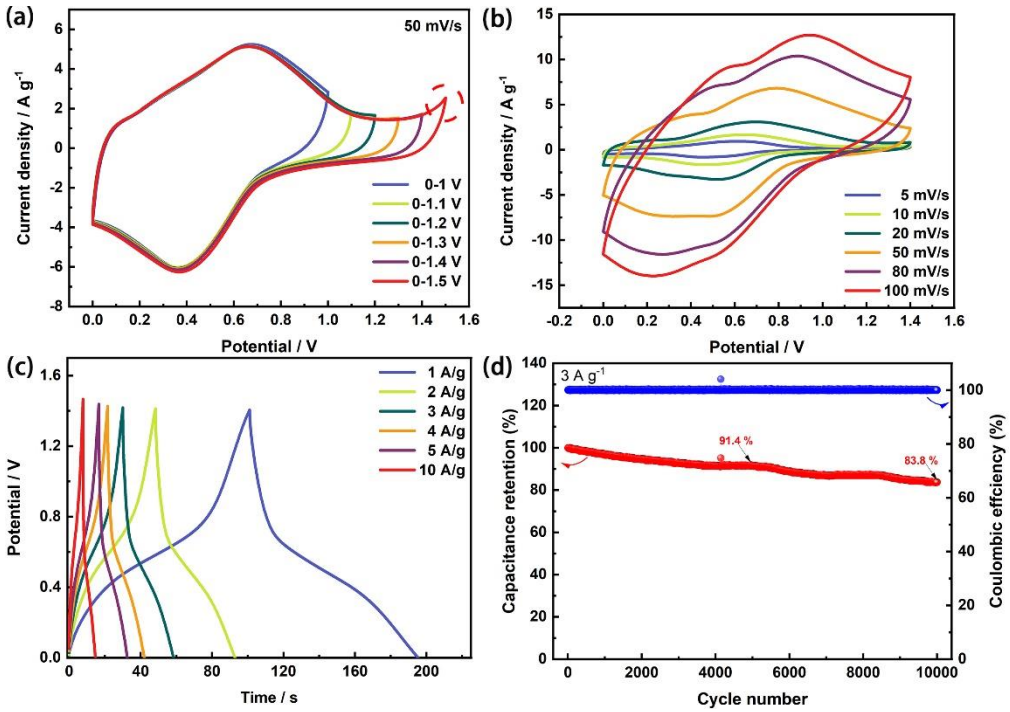

Figure 4.15. *Electrochemical performance of the as-assembled PYT/GN 4–5//A-$Ti_3C_2T_x$ ASC. (a) CV curves recorded at different potential windows. (b) CV curves at different scan rates. (c) GCD curves at various current densities. (d) Cycling life at 3 A g^{-1}.*[122]

Compared to the PYT/GN 4-5//A-$Ti_3C_2T_x$ ASC, the ones assembled with conducting polymers and A-$Ti_3C_2T_x$ exhibit a wider operation window and a higher energy density. The 2/1 PPYT/rGO//A-$Ti_3C_2T_x$ ASC shows a wide operation window upto 1.9 V with 1M H_2SO_4 as the electrolyte (Figure 4.16a). The ASC is measured with CV and GCD (Figures 4.16b and c) at various scan rates and current densities. Based on the mass loading, the 2/1 PPYT/rGO//A-$Ti_3C_2T_x$ ASC exhibits capacitances of 75.9, 73.1, 70.2, 68.9, 67.5, 61.4 F g^{-1} at current densities from 1 to 10 A g^{-1}, respectively. Moreover, after 15000 cycles, the 2/1 PPYT/rGO//A-$Ti_3C_2T_x$ ASC can still deliver 91.3% retention (Figure 4.16d). As for the 2/1 PPYTQ/rGO// A-$Ti_3C_2T_x$ ASC (Figure 4.17), it can also exhibit an operation window of 1.9 V. The specific capacitance of the 2/1 PPYT/rGO//A-$Ti_3C_2T_x$ ASC is 64.1, 59.5, 56.1, 53.9, 52.2, and 46.3 F g^{-1} at current densities of 1–10 A g^{-1}, according to the total mass of the cathode and anode. It can still deliver 95.1% retention after 15000 cycles at a current density of 5 A g^{-1}.

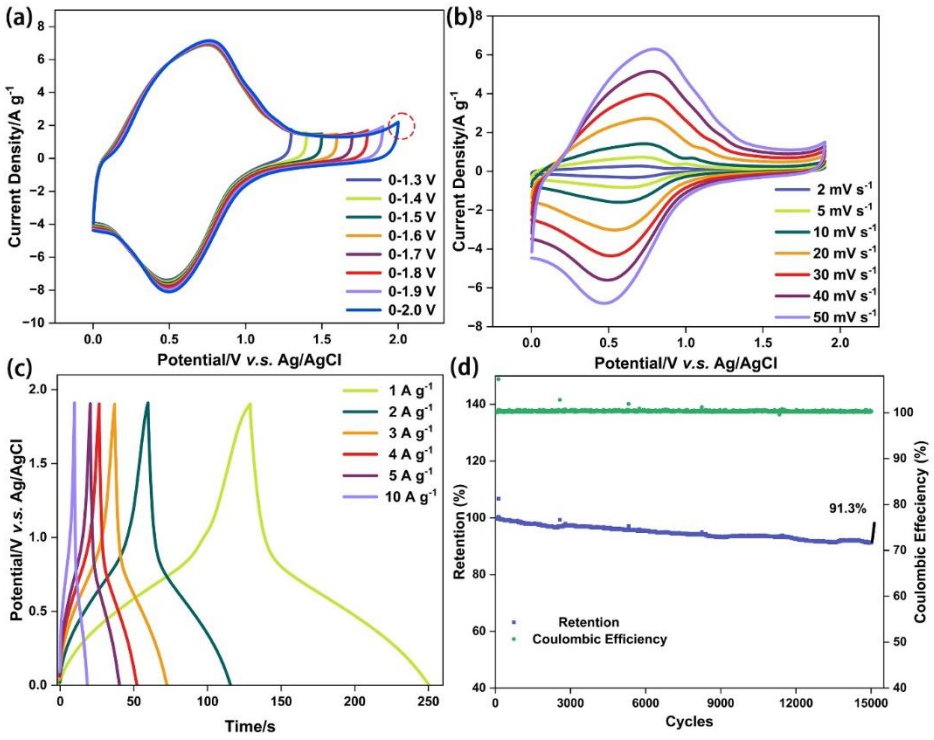

Figure 4.16. *Electrochemical performance of the as-assembled 2/1 PPYT/rGO//A-$Ti_3C_2T_x$ ASC. (a) CV curves recorded at different potential windows. (b) CV curves at different scan rates. (c) GCD curves at various current densities. (d) Cycling life at 5 A g^{-1}.*[123]

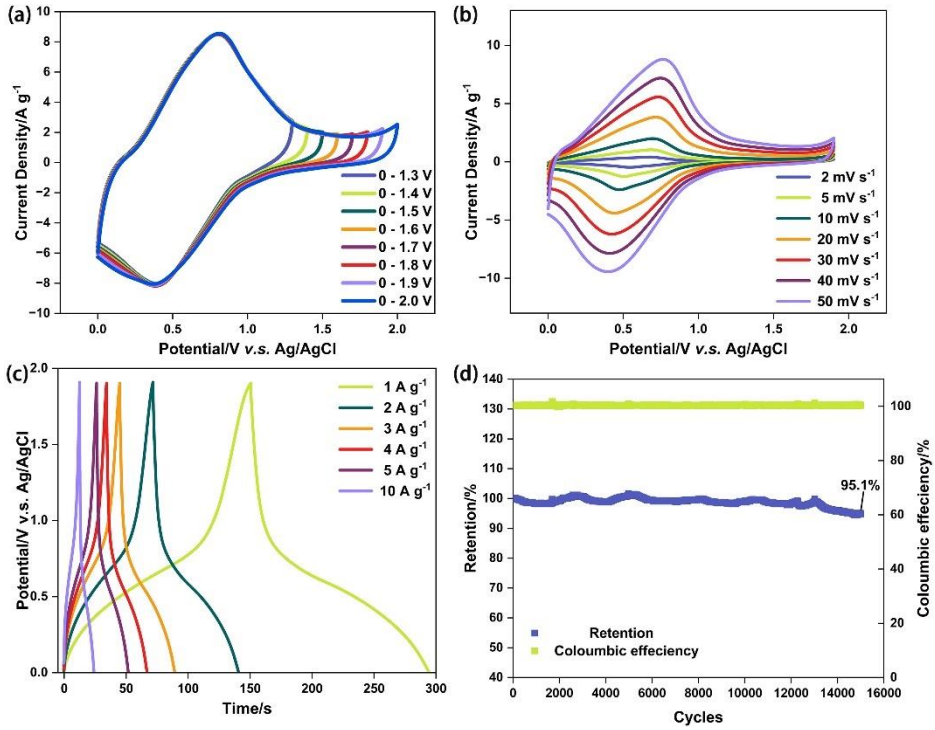

Figure 4.17. *Electrochemical performance of the as-assembled 2/1 PPYTQ/rGO//A-$Ti_3C_2T_x$ ASC. (a) CV curves recorded at different potential windows. (b) CV curves at different scan rates. (c) GCD curves at various current densities. (d) Cycling life at 5 A g^{-1}.*[123]

Owing to the wide operation window, the 2/1 PPYT/rGO//A-$Ti_3C_2T_x$ ASC exhibits a high energy density of 38.1 Wh kg^{-1} at a power density of 950 W kg^{-1}, while for the 2/1 PPYTQ/rGO//A-$Ti_3C_2T_x$ ASC, the energy density can reach 32.1 Wh kg^{-1}.

4.2. PYT-based donor-acceptor molecules and the interaction with graphene

Since PYT and phenazine are electron-deficient structures, carbazole is chosen as the donor to construct D-A systems. The synthesis of the D-A molecule starts by introducing halides to the 2 or 2, 7 positions of PYT as the coupling sites (Scheme 4.3). Then, the ketone groups are protected by acetalization before the Buchwald-Hartwig coupling to prevent them from coordinating with the metal catalyst. With the optimized ligand, the coupling reaction can reach a yield of 88% to afford the desired D-A skeleton. The following deprotection is achieved by adding 3a to a mixture of 9:1 TFA/water. The final product is obtained by the condensation reaction with 1,2-diamino-4,5-dimethoxybenzene.

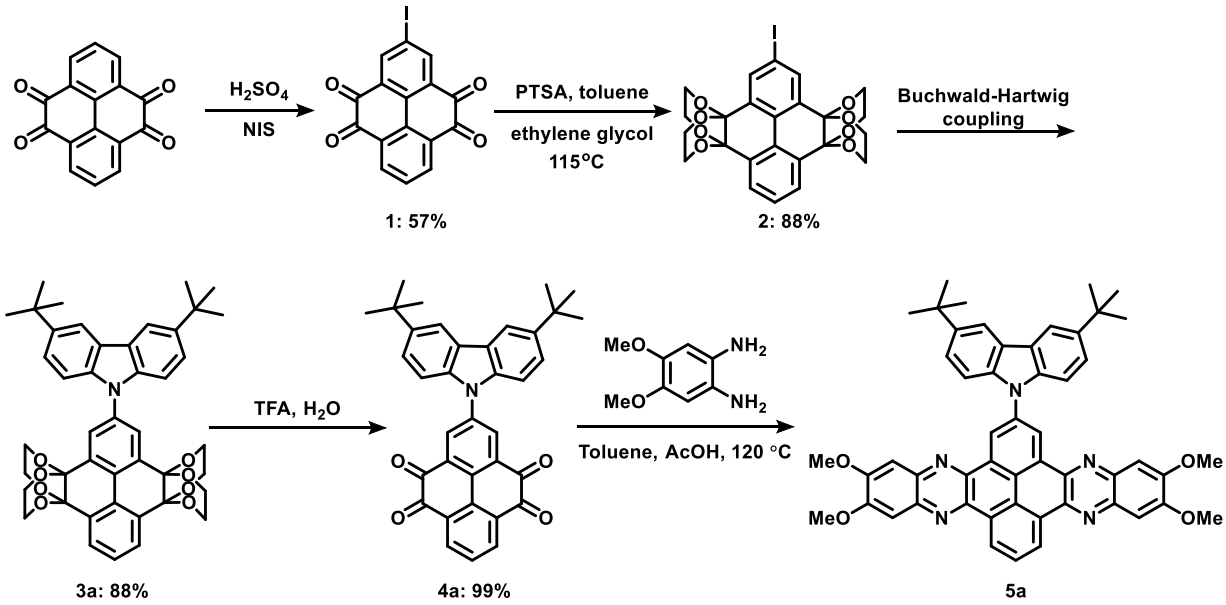

Scheme 4.3. *Synthetic route of the D-A system.*

4.2.1. Mechanism of Buchwald-Hartwig coupling

Pd-catalyzed amination of aryl halides and pseudohalides is a fundamental tool to form C(sp^2)–N bonds.[125-127] The mechanism of the reaction has been studied in depth throughout its development.

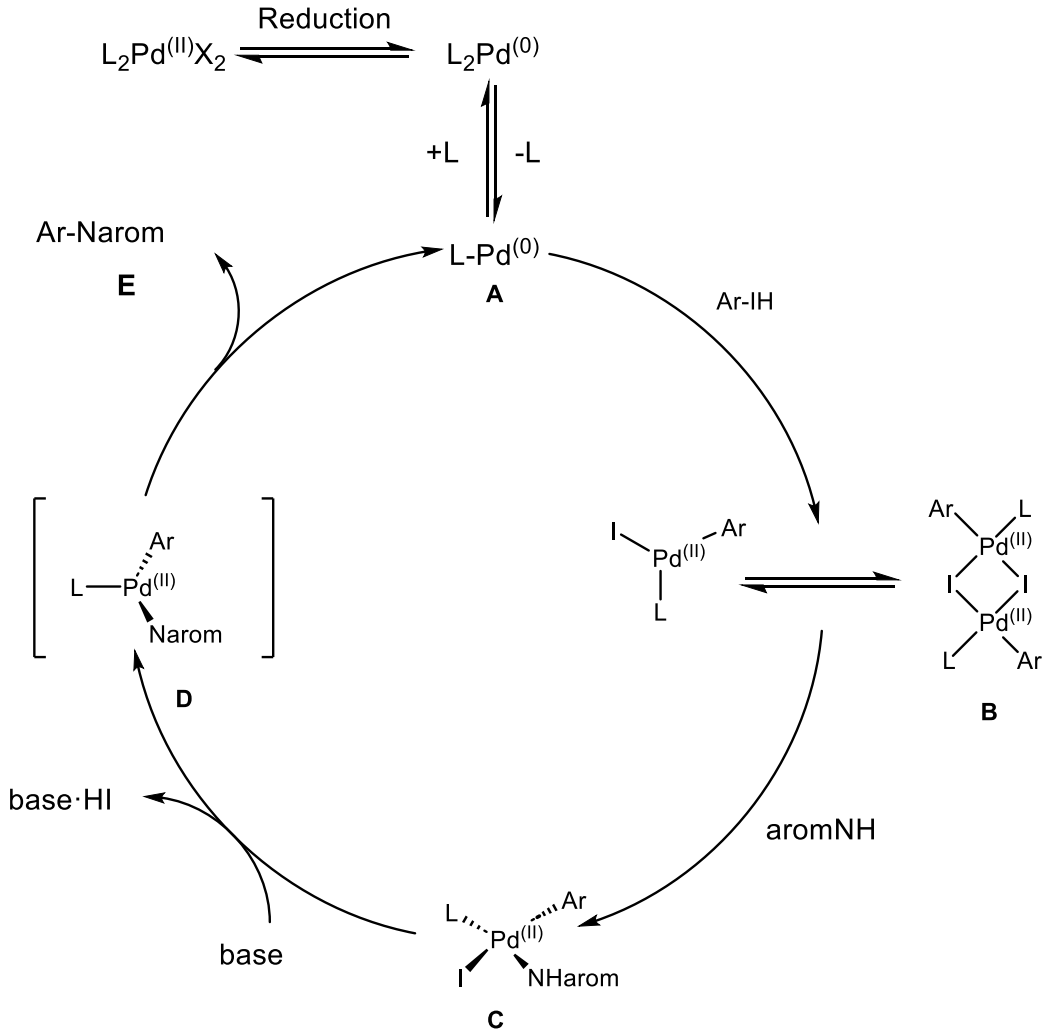

Scheme 4.4. *Catalytic cycle of Buchwald-Hartwig coupling.*

The catalytic cycle initiates with the reduction of the precatalyst Pd(II), leading to the formation of the Pd(0) catalyst (Scheme 4.4). Following the typical Pd-catalyzed mechanism, the Pd(0)-ligand complex A undergoes an oxidative addition with the aryl electrophile. In the next step, the aromatic amine (aromNH) coordinates with the metal complex C. In the presence of a base, the complex is deprotonated, and the final product E is generated after the reductive elimination of D.

4.2.2. Photophysical study of the interaction between the D-A system and rGO

The photophysics properties of the obtained D-A molecule are further investigated by UV/Vis absorption and photoluminescence spectroscopy (Figure 4.18). Meanwhile, rGO was added as a quencher to investigate the interaction with the D-A molecule. The D-A molecule shows a maximum absorption peak at 435 nm and the peak shows a redshift instead of a blueshift when rGO is added to the solution, indicating the interaction between the D-A molecule and rGO in

the ground state. Meanwhile, the emission of the molecule is quenched due to the potential energy/electron transfer between the two species. The process of the interaction will be further investigated in the future work.

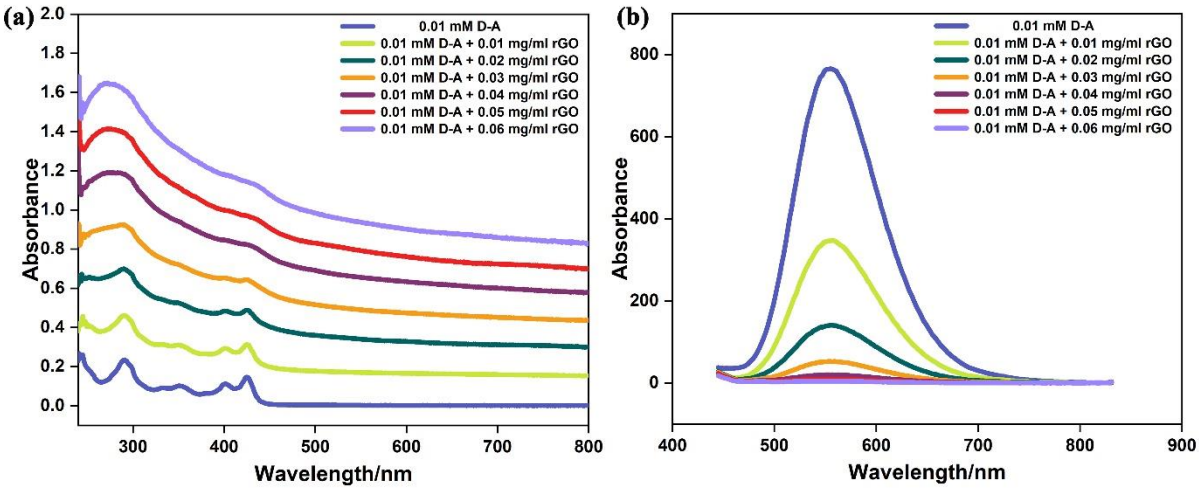

Figure 4.18. *UV/Vis absorption (a) and PL (b) spectra by titration between the D-A molecule and rGO (0.01-0.06 mg/ml, 10 µl each time) in chloroform. The concentration of the D-A molecule: 10 µM.*

5. Conclusion and outlook

This thesis presents a comprehensive investigation of two types of organic functional materials for applications in energy storage devices, along with an exploration of the interaction between polycyclic aromatic hydrocarbon donor-acceptor systems and 2D materials. The resulting materials have been evaluated from multiple perspectives, aiming to guide the design and synthesis of organic energy storage and optoelectronic materials.

In Paper I, we developed two types of PYT/rGO cathode materials capable of achieving a maximum specific capacitance of 711 A g^{-1} at a current density of 1 A g^{-1}. Interestingly, compared to the rGO with a higher reduction degree, the less reduced GO exhibited better electrochemical performance.

In Paper II, we designed and synthesized two conductive polymers of infinite rigid π-systems and polymers of π-systems linked by single bonds. Spectrophotometric titration revealed different assembly behaviours between the conducting polymers and rGO, providing valuable insights for the design of organic electrode materials. The polymer/rGO nanocomposite electrode demonstrated a high specific capacitance of 603 F g^{-1}. Moreover, the assembled ASC exhibited an energy density of 38.1 Wh kg^{-1} at a power density of 950 W kg^{-1}, with a wide operational window of 1.9 V in 1 M H_2SO_4.

In future research, we aim to design and synthesize novel redox materials based on the PYT system. Given the intriguing structure of PYT and the polymers discussed earlier, our focus will be on investigating their electrochemical behaviours in aqueous electrolytes with redox additives.

We have completed the synthesis of donor-acceptor polycyclic aromatic hydrocarbon molecules and conducted preliminary investigations into their photophysical properties. Future work will involve the measurement of time-resolved spectroscopy, with the possibility of implementing further structural modifications based on the current structure.

6. Acknowledgments

The work can’t be finished without the help and support from the people around me. I especially want to mention some of you:

I appreciate my supervisor, Xiaoyan Zhang, who has provided me with invaluable and serious insights into research and has guided my studies over the past years. I look forward to continuing the journey together. Also, my co-supervisor Gunnar Westman for the generous encouragement and help.

My examiner, Jerker Mårtensson, is always ready for the exciting scientific discussion. Thank you for that. And being in your lecture is always interesting. As well as Nina and Lars, working with you on the same floor and in the courses is enjoyable.

I really appreciate Ishan, Mangmang, and Zenghua as labmates, offering me help with lab management and excellent working atomsphere.

I would also thank the current and former colleagues on the 9^{th} floor for the wonderful discussion, nice fika, and the international party.

7. Experimental section

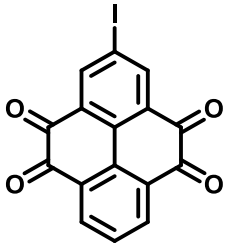

2-iodopyrene-4,5,9,10-tetraone (1)

15 mL of concentrated sulfuric acid (98%) was added to a 50 mL round bottom flask. Then, 262 mg (1.0 mmol) of pyrenetetrone and 270 mg of *N*-iodosuccinimide (1.5 mmol) were added to the reaction. The reaction mixture was allowed to stir at room temperature for 1 h before the temperature was raised to 50 °C in an oil bath and allowed to react for an additional 2 hours. Subsequently, the mixture was poured into 40 mL of ice water and neutralized with sodium bicarbonate. The crude product was then dried under vacuum and purified using column chromatography, resulting in the isolation of 221 mg of the target molecule with a yield of 57% (eluent: pure DCM-5% EA in DCM). ^{1}H NMR (400 MHz, $CDCl_3$): δ 8.79 (s, 2H), 8.52 (d, 2H, *J* = 7.8 Hz), 7.75 (t, 2H, *J* = 7.8 Hz).

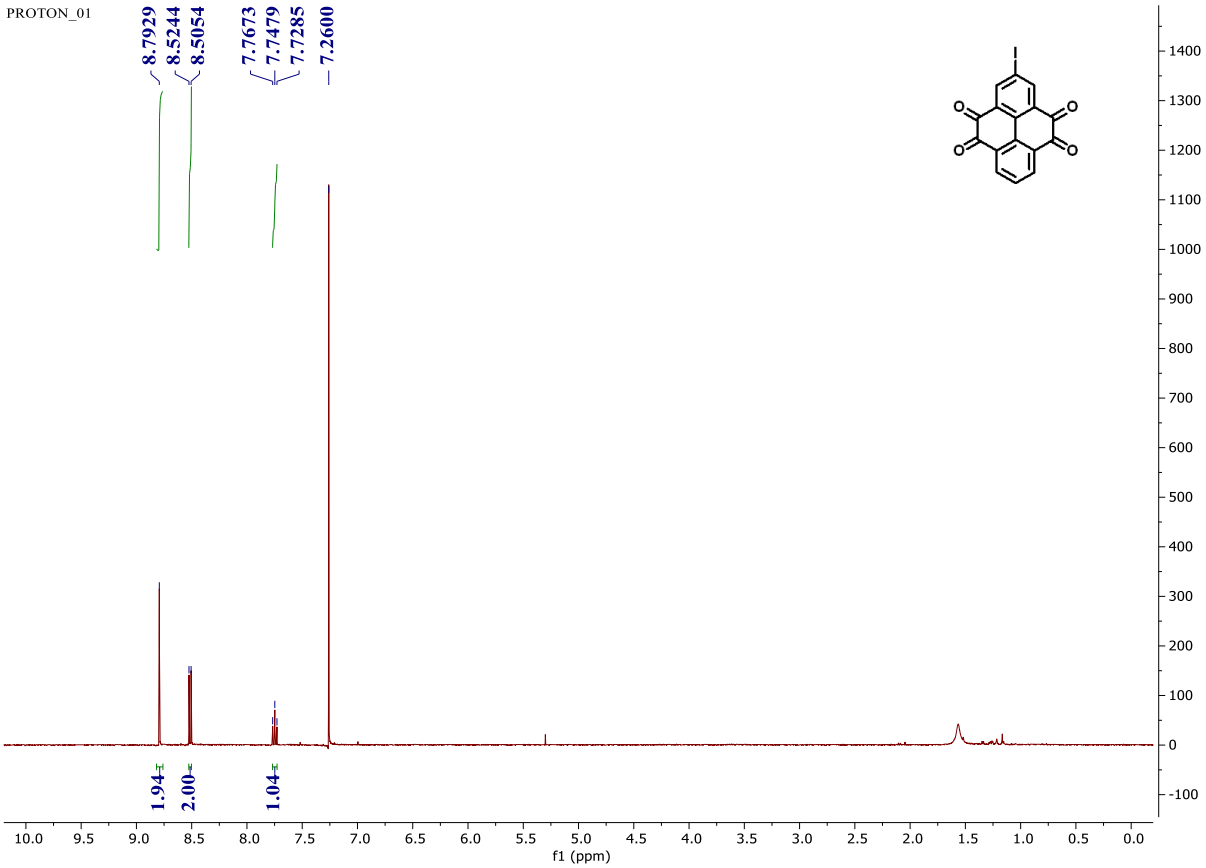

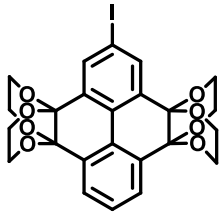

2-iodo-5,6,12,13-tetrahydro-3b,7a:10b,14a-bis(epoxyethanooxy)pyreno[4,5-b:9,10-b']bis([1,4]dioxine) (2)

To a 25 mL round bottom flask, 68.2 mg (0.2 mmol) of 2-iodopyrene-4,5,9,10-tetraone**,** 6.8 ml of toluene, 2.8 mL (0.05 mmol) of ethylene glycol and 34.2 mg (0.18 mmol) of p-toluenesulfonamide were added. The resulting reaction mixture was refluxed in a 125 ^{o}C oil bath for 20 hours. The reaction was cooled down to room temperature. Subsequently, toluene was removed by a rotary evaporator. The crude was filtered and washed with water and methanol until the solid was white (99.3 mg, 88%). ^{1}H NMR (400 MHz, $CDCl_3$): δ 8.09 (s, 2H), 7.75 (d, 2H, *J* = 7.7 Hz), 7.52 (t, 1H, *J* = 7.7 Hz), 4.20 (br, 6H), 3.67 (br, 6H).

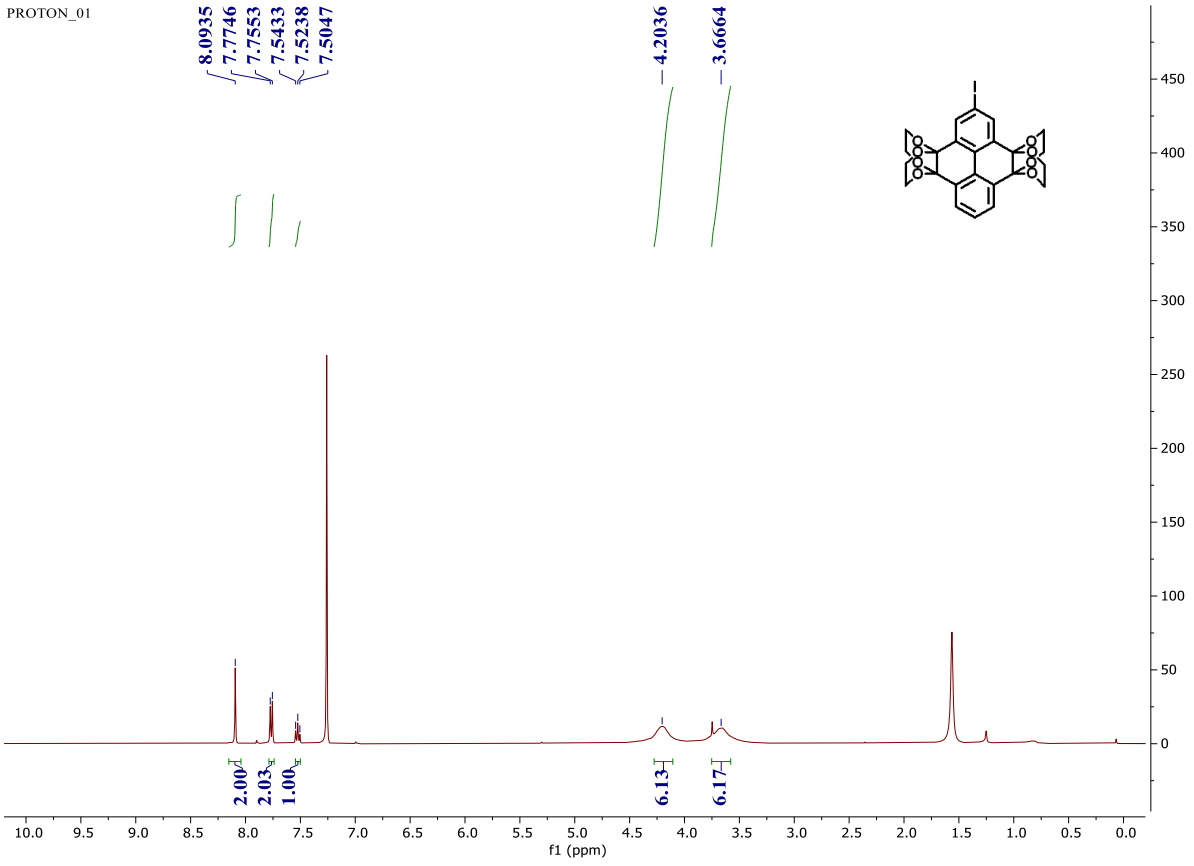

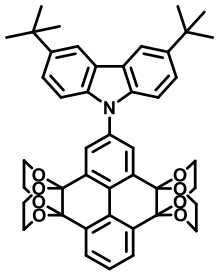

3,6-di-tert-butyl-9-(5,6,12,13-tetrahydro-3b,7a:10b,14a-bis(epoxyethanooxy)pyreno[4,5-b:9,10-b']bis([1,4]dioxine)-2-yl)-9H-carbazole (3a)

To a 50 mL three-necked round bottom flask, 35 mg (0.067 mmol) of 2-bromo-4,5,9,10-di(ethylene glycol)ketal-pyrene, 1.4 mg (0.0134 mmol) of $Pd_2(dba)_3 \cdot CH_3Cl$, 5.4 mg (0.0268 mmol) of $(t\text{-}Bu)_3P$, 22.6 mg (0.201 mmol) of KO*t*Bu, and 21mg (0.075 mmol) of 3,6-di-tert-butylcarbazole were added. Then, the three-necked R-B flask and the condenser were purged with nitrogen. Subsequently, the reaction mixture was stirred at 115 °C for 18 hours. The solvent was removed under reduced pressure. 42.2 mg product was obtained by flash chromatography with a yield of 88%. ^{1}H NMR (400 MHz, $CDCl_3$): δ 8.14 (m, 2H), 8.00 (s, 1H), 7.82 (d, 2H, *J* = 7.8 Hz), 7.54 (t, 1H, *J* = 7.8 Hz), 7.46 - 7.49 (m, 4H), 4.21 (br, 6H), 3.72 (br, 6H), 1.47 (s, 18H).

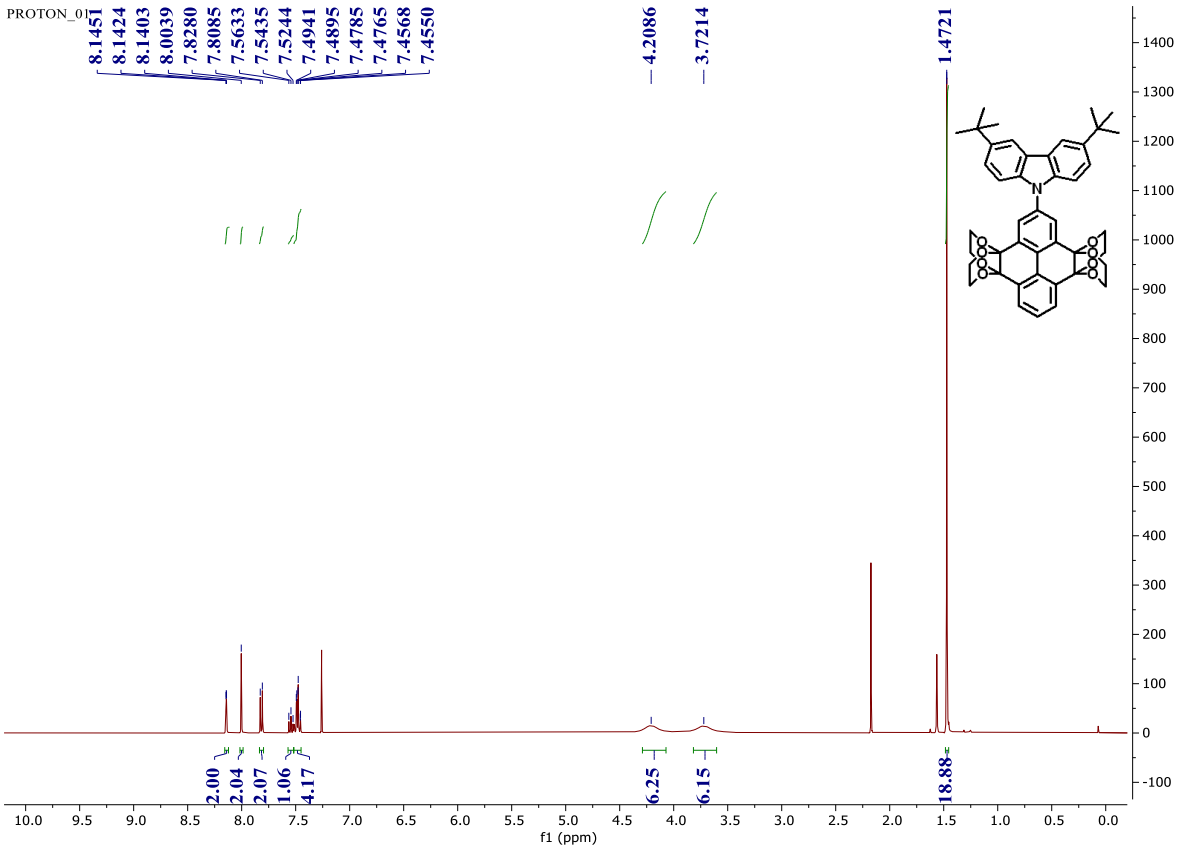

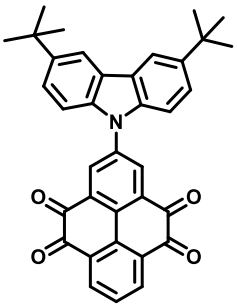

2-(3,6-di-tert-butyl-9H-carbazol-9-yl)pyrene-4,5,9,10-tetraone (4a)

32 mg (0.045 mmol) of PC-BKetal-Cbz-1 was added into a 25 mL R-B flask. Then, 5 mL of TFA/H_2O=9/1 solution was slowly added to the flask. The reaction mixture was stirred at room temperature. After 15 hours, the reaction solution was poured into crushed ice. Then the mixture was extracted with 3 × 10 mL of DCM, and dried with sodium sulfate. The solution was evaporated by rotavapor with a yield of 99%. ^{1}H NMR (400 MHz, $CDCl_3$): δ 8.74 (s, 2H), 8.55 (d, 2H, J = 7.8 Hz), 8.15 (d, 2H, J = 1.7 Hz), 7.74 (t, 1H, J = 7.8 Hz), 7.54 (dd, 2H, J_1 = 4.3 Hz, J_2 = 2.0 Hz), 7.44 (d, 2H, J = 8.7 Hz), 1.48 (s, 18H).

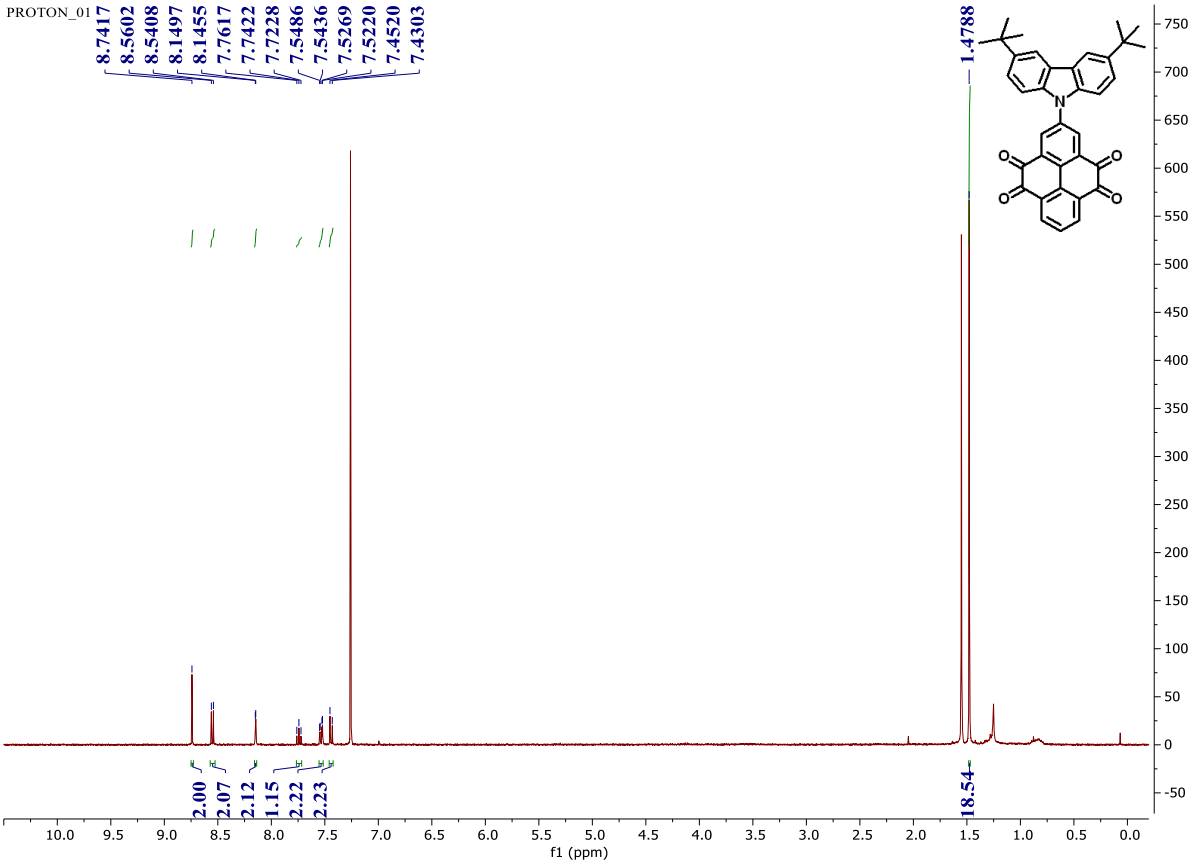

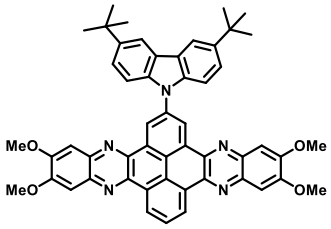

2-(3,6-di-tert-butyl-9H-carbazol-9-yl)-6,7,15,16-tetramethoxyquinoxalino[2',3':9,10]-phenanthro[4,5-abc]phenazine (5a)

118 mg (0.2 mmol) of 2-(3,6-di-tert-butyl-9H-carbazol-9-yl)pyrene-4,5,9,10-tetraone, 106 mg (0.44 mmol) of 4,5-dimethoxyl-1,2-phenyldiammonium chloride, 29 ml of toluene, and 29 ml of acetic acid were added into a 100 ml round-bottom flask. The mixture was stirred at 120 ℃ under a nitrogen atmosphere overnight. Subsequently, the solid was washed with 3 × 2 ml of methanol, 3 × 2 ml of ethyl acetate. The washing process involved 30 mins of sonication followed by 1 h centrifugation at a speed of 12000 r.p.m. The final product was dried in vacuum. ^{1}H NMR (400 MHz, $CDCl_3$): δ 9.88 (s, 2H), 9.68 (d, *J* = 7.9 Hz, 2H), 8.28 (d, *J* = 1.9 Hz, 2H), 8.23 (t, *J* = 7.9 Hz, 1H), 7.71 (d, *J* = 8.6 Hz, 2H), 7.63 (s, 2H), 7.58 (d, *J* = 1.9 Hz, 1H), 7.56 (s, 3H), 4.19 (s, 6H), 4.14 (s, 6H), 1.54 (s, 18H).

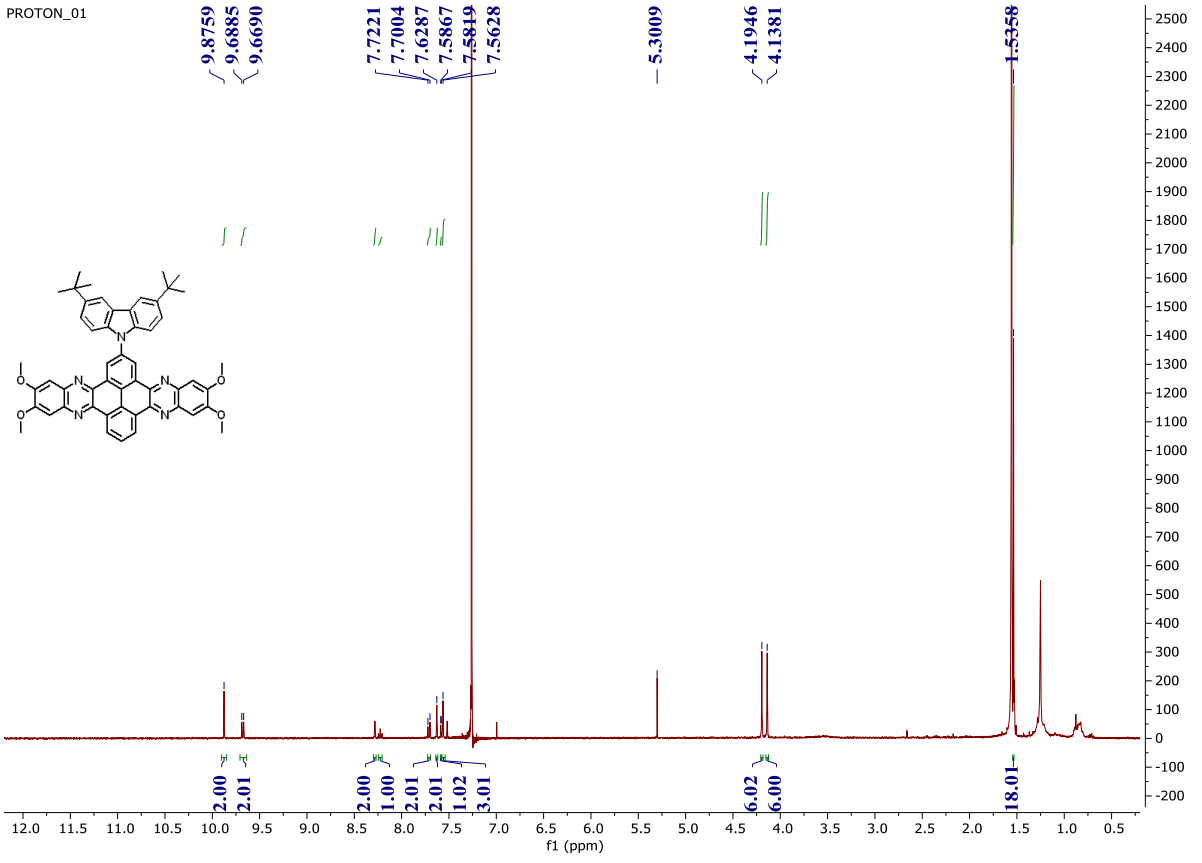

8. Reference

[1] A. Wainwright, *The Western Fells*, Frances Lincoln Limited, **2004**.
[2] O. Ruffhead, *The statutes at large, from the twentieth year of the reign of King George the second to the thirtith year of the reign of King George the second*, **1764**.
[3] K. S. Novoselov, A. K. Geim, S. V. Morozov, D. Jiang, Y. Zhang, S. V. Dubonos, I. V. Grigorieva, A. A. Firsov, *Science* **2004**, 306, 666.
[4] A. K. Geim, K. S. Novoselov, *Nature Materials* **2007**, 6, 183.
[5] A. A. Balandin, S. Ghosh, W. Bao, I. Calizo, D. Teweldebrhan, F. Miao, C. N. Lau, *Nano Letters* **2008**, 8, 902.
[6] H. Chen, M. B. Müller, K. J. Gilmore, G. G. Wallace, D. Li, *Advanced Materials* **2008**, 20, 3557.
[7] K. S. Novoselov, A. K. Geim, S. V. Morozov, D. Jiang, M. I. Katsnelson, I. V. Grigorieva, S. V. Dubonos, A. A. Firsov, *Nature* **2005**, 438, 197.
[8] M. D. Stoller, S. Park, Y. Zhu, J. An, R. S. Ruoff, *Nano Letters* **2008**, 8, 3498.
[9] A. Reina, X. Jia, J. Ho, D. Nezich, H. Son, V. Bulovic, M. S. Dresselhaus, J. Kong, *Nano Letters* **2009**, 9, 30.
[10] W. H. Lee, J. Park, Y. Kim, K. S. Kim, B. H. Hong, K. Cho, *Advanced Materials* **2011**, 23, 3460.
[11] S. Huh, J. Park, K. S. Kim, B. H. Hong, S. B. Kim, *ACS Nano* **2011**, 5, 3639.
[12] Y. Wang, Z. Li, J. Wang, J. Li, Y. Lin, *Trends in Biotechnology* **2011**, 29, 205.
[13] V. Chandra, J. Park, Y. Chun, J. W. Lee, I.-C. Hwang, K. S. Kim, *ACS Nano* **2010**, 4, 3979.
[14] R. Raccichini, A. Varzi, S. Passerini, B. Scrosati, *Nature Materials* **2015**, 14, 271.
[15] J. Zhu, D. Yang, Z. Yin, Q. Yan, H. Zhang, *Small* **2014**, 10, 3480.
[16] C.-Y. Su, A.-Y. Lu, Y. Xu, F.-R. Chen, A. N. Khlobystov, L.-J. Li, *ACS Nano* **2011**, 5, 2332.
[17] M. Lotya, Y. Hernandez, P. J. King, R. J. Smith, V. Nicolosi, L. S. Karlsson, F. M. Blighe, S. De, Z. Wang, I. T. McGovern, G. S. Duesberg, J. N. Coleman, *Journal of the American Chemical Society* **2009**, 131, 3611.
[18] S. Park, R. S. Ruoff, *Nature Nanotechnology* **2009**, 4, 217.
[19] Y. Zhu, M. D. Stoller, W. Cai, A. Velamakanni, R. D. Piner, D. Chen, R. S. Ruoff, *ACS Nano* **2010**, 4, 1227.
[20] Y. Shao, J. Wang, M. Engelhard, C. Wang, Y. Lin, *Journal of Materials Chemistry* **2010**, 20, 743.
[21] Z.-S. Wu, W. Ren, L. Gao, J. Zhao, Z. Chen, B. Liu, D. Tang, B. Yu, C. Jiang, H.-M. Cheng, *ACS Nano* **2009**, 3, 411.
[22] K. S. Kim, Y. Zhao, H. Jang, S. Y. Lee, J. M. Kim, K. S. Kim, J.-H. Ahn, P. Kim, J.-Y. Choi, B. H. Hong, *Nature* **2009**, 457, 706.
[23] S. Bae, H. Kim, Y. Lee, X. Xu, J.-S. Park, Y. Zheng, J. Balakrishnan, T. Lei, H. Ri Kim, Y. I. Song, Y.-J. Kim, K. S. Kim, B. Özyilmaz, J.-H. Ahn, B. H. Hong, S. Iijima, *Nature Nanotechnology* **2010**, 5, 574.
[24] J. Cai, C. A. Pignedoli, L. Talirz, P. Ruffieux, H. Söde, L. Liang, V. Meunier, R. Berger, R. Li, X. Feng, K. Müllen, R. Fasel, *Nature Nanotechnology* **2014**, 9, 896.
[25] M. Choucair, P. Thordarson, J. A. Stride, *Nature Nanotechnology* **2009**, 4, 30.
[26] S. Stankovich, R. D. Piner, S. T. Nguyen, R. S. Ruoff, *Carbon* **2006**, 44, 3342.
[27] J.-W. Jiang, H. S. Park, *Journal of Physics D: Applied Physics* **2014**, 47, 385304.
[28] Y. Shi, C. Hamsen, X. Jia, K. K. Kim, A. Reina, M. Hofmann, A. L. Hsu, K. Zhang, H. Li, Z.-Y. Juang, M. S. Dresselhaus, L.-J. Li, J. Kong, *Nano Letters* **2010**, 10, 4134.

[29] Q. Weng, X. Wang, X. Wang, Y. Bando, D. Golberg, *Chemical Society Reviews* **2016**, 45, 3989.
[30] A. Lipatov, H. Lu, M. Alhabeb, B. Anasori, A. Gruverman, Y. Gogotsi, A. Sinitskii, *Science Advances* **2018**, 4, eaat0491.
[31] Z. Xie, C. Xing, W. Huang, T. Fan, Z. Li, J. Zhao, Y. Xiang, Z. Guo, J. Li, Z. Yang, B. Dong, J. Qu, D. Fan, H. Zhang, *Advanced Functional Materials* **2018**, 28, 1705833.
[32] L.-B. Zhan, C.-L. Yang, M.-S. Wang, X.-G. Ma, *Applied Surface Science* **2020**, 530, 147137.
[33] M. Naguib, V. N. Mochalin, M. W. Barsoum, Y. Gogotsi, *Advanced Materials* **2014**, 26, 992.
[34] M. Quintana, K. Spyrou, M. Grzelczak, W. R. Browne, P. Rudolf, M. Prato, *ACS Nano* **2010**, 4, 3527.
[35] M. Quintana, A. Montellano, A. E. del Rio Castillo, G. V. Tendeloo, C. Bittencourt, M. Prato, *Chemical Communications* **2011**, 47, 9330.
[36] Z. Jin, T. P. McNicholas, C.-J. Shih, Q. H. Wang, G. L. C. Paulus, A. J. Hilmer, S. Shimizu, M. S. Strano, *Chemistry of Materials* **2011**, 23, 3362.
[37] T. A. Strom, E. P. Dillon, C. E. Hamilton, A. R. Barron, *Chemical Communications* **2010**, 46, 4097.
[38] C. K. Chua, M. Pumera, *Chemistry – An Asian Journal* **2012**, 7, 1009.
[39] W. Lai, J. Liu, L. Luo, X. Wang, T. He, K. Fan, X. Liu, *Chemical Communications* **2018**, 54, 10168.
[40] V. Georgakilas, J. N. Tiwari, K. C. Kemp, J. A. Perman, A. B. Bourlinos, K. S. Kim, R. Zboril, *Chemical Reviews* **2016**, 116, 5464.
[41] J. Zhan, Z. Lei, Y. Zhang, *Chem* **2022**, 8, 947.
[42] D. A. Lashof, D. R. Ahuja, *Nature* **1990**, 344, 529.
[43] S. Chu, Y. Cui, N. Liu, *Nature Materials* **2017**, 16, 16.
[44] A. Polman, M. Knight, E. C. Garnett, B. Ehrler, W. C. Sinke, *Science* **2016**, 352, aad4424.
[45] S. Chu, A. Majumdar, *Nature* **2012**, 488, 294.
[46] W. Colglazier, *Science* **2015**, 349, 1048.
[47] J. M. Gonzalez, J. E. Tomlinson, E. A. Martínez Ceseña, M. Basheer, E. Obuobie, P. T. Padi, S. Addo, R. Baisie, M. Etichia, A. Hurford, A. Bottacin-Busolin, J. Matthews, J. Dalton, D. M. Smith, J. Sheffield, M. Panteli, J. J. Harou, *Nature Sustainability* **2023**, 6, 415.
[48] R. Wang, M. Yao, Z. Niu, *InfoMat* **2020**, 2, 113.
[49] J. R. Miller, P. Simon, *Science* **2008**, 321, 651.
[50] Z. Zhu, T. Jiang, M. Ali, Y. Meng, Y. Jin, Y. Cui, W. Chen, *Chemical Reviews* **2022**, 122, 16610.
[51] T. Christen, M. W. Carlen, *Journal of Power Sources* **2000**, 91, 210.
[52] Y. Chen, Y. Kang, Y. Zhao, L. Wang, J. Liu, Y. Li, Z. Liang, X. He, X. Li, N. Tavajohi, *Journal of Energy Chemistry* **2021**, 59, 83.
[53] P. Lyu, X. Liu, J. Qu, J. Zhao, Y. Huo, Z. Qu, Z. Rao, *Energy Storage Materials* **2020**, 31, 195.
[54] P. Simon, Y. Gogotsi, *Nature Materials* **2008**, 7, 845.
[55] E. Frackowiak, *Physical Chemistry Chemical Physics* **2007**, 9, 1774.
[56] H. Helmholtz, *Annalen der Physik* **1853**, 165, 353.
[57] M. Gouy, *Journal of Physics: Theories and Applications* **1910**, 9, 457.
[58] O. Stern, *Zeitschrift für Elektrochemie und angewandte physikalische Chemie* **1924**, 30, 508.
[59] D. C. Grahame, *Chemical Reviews* **1947**, 41, 441.
[60] E. Frackowiak, F. Béguin, *Carbon* **2002**, 40, 1775.
[61] D. Qu, H. Shi, *Journal of Power Sources* **1998**, 74, 99.

[62] L. J. Wang, M. F. El‐Kady, S. Dubin, J. Y. Hwang, Y. Shao, K. Marsh, B. McVerry, M. D. Kowal, M. F. Mousavi, R. B. Kaner, *Advanced Energy Materials* **2015**, 5, 1500786.
[63] J. Lin, C. Zhang, Z. Yan, Y. Zhu, Z. Peng, R. H. Hauge, D. Natelson, J. M. Tour, *Nano Letters* **2013**, 13, 72.
[64] S. Trasatti, G. Buzzanca, *Journal of Electroanalytical Chemistry and Interfacial Electrochemistry* **1971**, 29, A1.
[65] B. Liu, R. Bo, M. Taheri, I. Di Bernardo, N. Motta, H. Chen, T. Tsuzuki, G. Yu, A. Tricoli, *Nano Letters* **2019**, 19, 4391.
[66] J. Chen, Y. Liu, A. I. Minett, C. Lynam, J. Wang, G. G. Wallace, *Chemistry of Materials* **2007**, 19, 3595.
[67] H.-g. Wang, Q. Li, Q. Wu, Z. Si, X. Lv, X. Liang, H. Wang, L. Sun, W. Shi, S. Song, *Advanced Energy Materials* **2021**, 11, 2100381.
[68] X. Yang, Y. Hu, N. Dunlap, X. Wang, S. Huang, Z. Su, S. Sharma, Y. Jin, F. Huang, X. Wang, S.-h. Lee, W. Zhang, *Angewandte Chemie International Edition* **2020**, 59, 20385.
[69] B. Huskinson, M. P. Marshak, C. Suh, S. Er, M. R. Gerhardt, C. J. Galvin, X. Chen, A. Aspuru-Guzik, R. G. Gordon, M. J. Aziz, *Nature* **2014**, 505, 195.
[70] M. Wang, F. Zhang, C.-S. Lee, Y. Tang, *Advanced Energy Materials* **2017**, 7, 1700536.
[71] T. P. Nguyen, A. D. Easley, N. Kang, S. Khan, S.-M. Lim, Y. H. Rezenom, S. Wang, D. K. Tran, J. Fan, R. A. Letteri, X. He, L. Su, C.-H. Yu, J. L. Lutkenhaus, K. L. Wooley, *Nature* **2021**, 593, 61.
[72] S. Zhang, N. Pan, *Advanced Energy Materials* **2015**, 5, 1401401.
[73] N. Choudhary, C. Li, J. Moore, N. Nagaiah, L. Zhai, Y. Jung, J. Thomas, *Advanced Materials* **2017**, 29, 1605336.
[74] Y. Shao, M. F. El-Kady, J. Sun, Y. Li, Q. Zhang, M. Zhu, H. Wang, B. Dunn, R. B. Kaner, *Chemical Reviews* **2018**, 118, 9233.
[75] F. Bonaccorso, Z. Sun, T. Hasan, A. C. Ferrari, *Nature Photonics* **2010**, 4, 611.
[76] Z. Weng, S. C. Dixon, L. Y. Lee, C. J. Humphreys, I. Guiney, O. Fenwick, W. P. Gillin, *Advanced Optical Materials* **2022**, 10, 2101675.
[77]L. M. Cavinato, K. Yamaoka, S. Lipinski, V. Calvi, D. Wehenkel, R. van Rijn, K. Albrecht, R. D. Costa, *Advanced Functional Materials* **2023**, 33, 2302483.
[78] J. Wu, H. Lin, D. J. Moss, K. P. Loh, B. Jia, *Nature Reviews Chemistry* **2023**, 7, 162.
[79] Y. Chen, Y.-Y. Yue, S.-R. Wang, N. Zhang, J. Feng, H.-B. Sun, *Advanced Electronic Materials* **2019**, 5, 1900247.
[80] Y. Xiong, Q. Liao, Z. Huang, X. Huang, C. Ke, H. Zhu, C. Dong, H. Wang, K. Xi, P. Zhan, F. Xu, Y. Lu, *Advanced Materials* **2020**, 32, 1907242.
[81] F. Bonaccorso, N. Balis, M. M. Stylianakis, M. Savarese, C. Adamo, M. Gemmi, V. Pellegrini, E. Stratakis, E. Kymakis, *Advanced Functional Materials* **2015**, 25, 3870.
[82] Y. Sun, W. Zhang, H. Chi, Y. Liu, C. L. Hou, D. Fang, *Renewable and Sustainable Energy Reviews* **2015**, 43, 973.
[83] F. W. Low, C. W. Lai, *Renewable and Sustainable Energy Reviews* **2018**, 82, 103.
[84] Z. Liu, Y. Wang, X. Zhang, Y. Xu, Y. Chen, J. Tian, *Applied Physics Letters* **2009**, 94.
[85] B. Guo, Q. l. Xiao, S. h. Wang, H. Zhang, *Laser & Photonics Reviews* **2019**, 13, 1800327.
[86] Z. Sun, A. Martinez, F. Wang, *Nature Photonics* **2016**, 10, 227.
[87] S. Yu, X. Wu, Y. Wang, X. Guo, L. Tong, *Advanced Materials* **2017**, 29, 1606128.
[88] Q. Bao, H. Zhang, B. Wang, Z. Ni, C. H. Y. X. Lim, Y. Wang, D. Y. Tang, K. P. Loh, *Nature Photonics* **2011**, 5, 411.
[89] W. Song, C. He, W. Zhang, Y. Gao, Y. Yang, Y. Wu, Z. Chen, X. Li, Y. Dong, *Carbon* **2014**, 77, 1020.
[90] J. Zhu, Y. Li, Y. Chen, J. Wang, B. Zhang, J. Zhang, W. J. Blau, *Carbon* **2011**, 49, 1900.

[91] A. Ganesan, A. Husain, M. Sebastian, S. Makhseed, *Dyes and Pigments* **2021**, 196, 109794.
[92] A. J. Clancy, M. K. Bayazit, S. A. Hodge, N. T. Skipper, C. A. Howard, M. S. P. Shaffer, *Chemical Reviews* **2018**, 118, 7363.
[93] D. Dasler, R. A. Schäfer, M. B. Minameyer, J. F. Hitzenberger, F. Hauke, T. Drewello, A. Hirsch, *Journal of the American Chemical Society* **2017**, 139, 11760.
[94] M. Volland, P. Zhou, L. Wibmer, R. Häner, S. Decurtins, S.-X. Liu, D. M. Guldi, *Nanoscale* **2019**, 11, 1437.
[95] E. Clar, in *Mobile Source Emissions Including Policyclic Organic Species*, (Eds: D. Rondia, M. Cooke, R. K. Haroz), Springer Netherlands, Dordrecht **1983**.
[96] K. Fukui, T. Yonezawa, H. Shingu, *The Journal of Chemical Physics* **2004**, 20, 722.
[97] P. P. Fu, H. M. Lee, R. G. Harvey, *The Journal of Organic Chemistry* **1980**, 45, 2797.
[98] M. Schroeder, *Chemical Reviews* **1980**, 80, 187.
[99] A. J. Bard, L. R. Faulkner, H. S. White, *Electrochemical Methods: Fundamentals and Applications*, John Wiley & Sons, **2022**.
[100] T. Liu, W. G. Pell, B. E. Conway, *Electrochimica Acta* **1997**, 42, 3541.
[101] D. A. Bograchev, Y. M. Volfkovich, S. Martemianov, *Journal of Electroanalytical Chemistry* **2023**, 935, 117322.
[102] P. Simon, Y. Gogotsi, B. Dunn, *Science* **2014**, 343, 1210.
[103] P. L. Taberna, P. Simon, J. F. Fauvarque, *Journal of the Electrochemical Society* **2003**, 150, A292.
[104] M. F. Dupont, A. F. Hollenkamp, S. W. Donne, *Journal of the Electrochemical Society* **2014**, 161, A648.
[105] B.-A. Mei, O. Munteshari, J. Lau, B. Dunn, L. Pilon, *The Journal of Physical Chemistry C* **2018**, 122, 194.
[106] T. S. Mathis, N. Kurra, X. Wang, D. Pinto, P. Simon, Y. Gogotsi, *Advanced Energy Materials* **2019**, 9, 1902007.
[107] R. Kötz, M. Carlen, *Electrochimica Acta* **2000**, 45, 2483.
[108] C.-L. Liu, W.-S. Dong, G.-P. Cao, J.-R. Song, L. Liu, Y.-S. Yang, *Journal of Electroanalytical Chemistry* **2007**, 611, 225.
[109] I. Yang, S.-G. Kim, S. H. Kwon, M.-S. Kim, J. C. Jung, *Electrochimica Acta* **2017**, 223, 21.
[110] C. Lei, F. Markoulidis, Z. Ashitaka, C. Lekakou, *Electrochimica Acta* **2013**, 92, 183.
[111] C. Portet, G. Yushin, Y. Gogotsi, *Carbon* **2007**, 45, 2511.
[112] Y.-R. Nian, H. Teng, *Journal of Electroanalytical Chemistry* **2003**, 540, 119.
[113] J. Hu, D. Zhang, F. W. Harris, *The Journal of Organic Chemistry* **2005**, 70, 707.
[114] R. B. Choudhary, S. Ansari, B. Purty, *Journal of Energy Storage* **2020**, 29, 101302.
[115] F. Fusalba, P. Gouérec, D. Villers, D. Bélanger, *Journal of the Electrochemical Society* **2001**, 148, A1.
[116] Y. T. Tan, F. Ran, L. R. Wang, L. B. Kong, L. Kang, *Journal of Applied Polymer Science* **2013**, 127, 1544.
[117] D. Dhawale, A. Vinu, C. Lokhande, *Electrochimica Acta* **2011**, 56, 9482.
[118] R. Oraon, A. De Adhikari, S. K. Tiwari, S. Bhattacharyya, G. C. Nayak, *RSC Advances* **2016**, 6, 64271.
[119] G. A. Snook, P. Kao, A. S. Best, *Journal of Power Sources* **2011**, 196, 1.
[120] A. M. Bryan, L. M. Santino, Y. Lu, S. Acharya, J. M. D'Arcy, *Chemistry of Materials* **2016**, 28, 5989.
[121] C. Wang, R. Li, Y. Zhu, Y. Wang, Y. Lin, L. Zhong, H. Chen, Z. Tang, H. Li, F. Liu, C. Zhi, H. Lv, *Advanced Energy Materials* **2024**, 14, 2302495.
[122] M. Shi, C. Peng, X. Zhang, *Small* **2023**, 19, 2301449.

[123] C. Peng, C. Guo, Y. Wang, Y. Li, X. Zhang, *Advanced Energy and Sustainability Research*, 2300217.
[124] J. Zhou, Q. Kang, S. Xu, X. Li, C. Liu, L. Ni, N. Chen, C. Lu, X. Wang, L. Peng, X. Guo, W. Ding, W. Hou, *Nano Research* **2022**, 15, 285.
[125] J. F. Hartwig, *Angewandte Chemie International Edition* **1998**, 37, 2046.
[126] J. P. Wolfe, S. Wagaw, J.-F. Marcoux, S. L. Buchwald, *Accounts of Chemical Research* **1998**, 31, 805.
[127] D. S. Surry, S. L. Buchwald, *Chemical Science* **2011**, 2, 27.